High Index Contrast Polymer Optical Waveguides

M.Sc. Thesis

by

Asael Adler

This work was done under the supervision of

Dr. Dan Marom

The Selim and Rachel Benin School of Engineering,

The Hebrew University of Jerusalem.

December 28, 2010

Acknowledgments

I want to thank my advisor, Dr. Dan Marom, for his support throughout my Master studies. His guidance was a cornerstone throughout my research. I want to thank Yaron Glazer for his help and support. His support in the initial stages of my master has been very important to me and the progress of my project. Very special thanks go to Jonathan Dunayevsky and Amitay Rudnick for being good friends and always being ready for a scientific discussion. I also want to thank all my others group members: David Sinefeld, Drori Shayovitz and Moran Bin-Nun for their friendship and for sharing their knowledge with me.

Additionally, I am grateful to the staff at the Nano Center and especially to Noa Mazurski for her help and constant support.

I would like to thank my parents for giving me the best education possible and the necessary tools to reach this point in my career. I also thank my brothers and sister for being so amazing in everything.

Finally, I would like to give a very special thanks to my girlfriend, Irena, for her love and support.

Abstract

This thesis investigated the realization of a polymer waveguiding material platform based on PFCB guiding core and Cytop cladding, which were chosen due to their intrinsic low material losses and relative high index contrast. The PFCB core material was also chosen due to its ability to accept semiconductor nanocrystal dopants, which are the long term objective beyond the scope of this research thesis.

The work focused on waveguide fabrication in PFCB polymer, in highly confined geometries using Cytop as the outer cladding material, which is a material platform I developed in the course of the last few years. Waveguides were fabricated as triple-layer stack geometry. This polymer combination offers a high index contrast Än of ~10%, which allows single mode operation with mode waist of 1.88ìm. The fabrication sequences were modified from the standards suggested in the literature, to accommodate a temperature limitation of 150C in support of our future plan to dope the waveguide core with nanocrystals which cannot tolerate elevated temperatures. The main challenge during the work was to cope with different thermal expansion coefficients between the hard mask layer (SiO2) and the PFCB. This required me to add 1.5ìm Cytop layer beneath the oxide hard mask, which reduced the stress at the hard mask.

The fabricated waveguides were characterized for propagation losses and bend loss. The propagation loss measurements gave losses of 1.06dB/cm at 1.55μm wavelength which is higher than the theoretical value of 0.29dB/cm due to sidewall roughness of the channel waveguides. Bend loss measurement was evaluated using racetrack resonators which gave bend loss of 3.75dB/cm (350μm radius bend) at an erroneous core dimensions of 0.85ìm×1.5ìm (as opposed to our 1.5ìm×1.5ìm target), which made the waveguide mode more sensitive to the sidewall roughness. Both these parameters are projected to improve after further processing refinement.

תקציר

התזה חוקרת פלטפורמה של מוליך גל הבנוי מחומרים פולימרים שמבוססים על Cytop ו PFCB, בעלי הפסדים נמוכים וניגוד גבוה במקדם השבירה. ליבת ה PFCB נבחרה עקב היכולת שלו לקבל ננו קריסטלים שזוהי המטרה שמעבר לתיזה הזו.

העבודה מתמקדת בהתקן אשר ליבתו מורכבת מפולימר PFCB בגאומטריה צפופה כאשר הפולימר Cytop משמש כמעטפת, פלטפורמת חומר זו פותחה במהלך השנים האחרונות. מולכי הגל יוצרו בגאומטרית 3 שכבות. קומבנצית פולימר זו מאפשרת ניגוד גבוה במקדם השבירה Δn של ~ 10% אשר מאפשרת עבודה בתחום אופן יחיד עם מותן של 1.88µm. תהליך היצור הותאם לטמפרטורה של 150 מעלות כדי שנוכל לסמם בעתיד את הליבה של מוליך הגל בננו חלקים אשר לא מסוגלים לשרוד טמפרטורה כזאת.במהלך תהליך היצור נדרשה התמודדת עם שינוים במקדם ההתפשטות הטרמי בין מסכת האוקסיד לבין פולימר PFCB. בעיה זאת נפתרה בעזרת הוספת 1.5µm של שכבת פולמר Cytop שהורידה את הלחצים על שכבת האוקסיד.

הפסדי מוליך הגל אשר נמדדו בעזרת שיטת פברי-פרו נתנו 1.06dB/cm באורך גל של 1.55µm. תוצאות אלו גבוהות מהערכים התיאורטיים עכב הקירות המספוסים של מוליך הגל.הפסדי הכיפוף נמדדו בעזרת מספר טבעות רזוננס בעלי פרמטרים שונים. המדידות הראו הפסדים של 3.75dB/cm (350µm רדיוס כיפוף) עבור מוליך גל בעל ממדים שגוים של 0.85µm×1.5µm (בניגוד ליעד של 1.5µm×1.5µm),אשר גרם למוליך גל להיות יותר רגיש לקירות המחוספסים. אנחנו מתכוונים לתקן את הבעיה בעזרת תכנון מסכה חדשה.

Table of Contents

1. Theoretical Background

1.1. Optical Waveguide Theory

Planar optical waveguides are the key devices to construct integrated optical circuits. Generally rectangular waveguides consist from dielectric core surrounded by a dielectric cladding with a lower reflective index. There are two approaches treating light wave propagation in optical waveguide. In the first approach each mode is associated with light rays at a discrete angle of propagation. Here we describe the formation of modes with the ray picture in slab waveguide. For the second approach we will use Maxwell's equations with boundary conditions to obtain the different modes of propagation in a rectangular waveguide [1].

1.1.1. Slab Waveguide and Basic Parameters

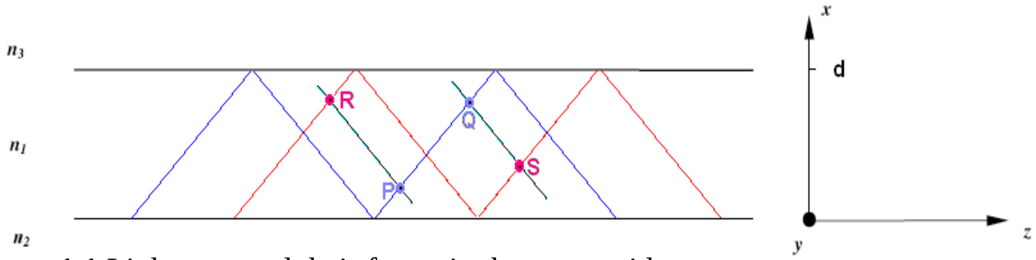

Figure 1.1 Light rays and their fronts in the waveguide.

The condition for total internal reflection at the core-cladding interface is given by the critical angel θ_c

$$\theta_{c2} = \arcsin\left(\frac{n_2}{n_1}\right), \theta_{c3} = \arcsin\left(\frac{n_3}{n_1}\right) \tag{1.1}$$

$$n_1 > n_2 \geq n_3$$

We can see from figure 1.1 that the optical paths PQ and RS should be equal, or their difference should be an integral multiple of 2π.The phase-matching condition for the optical paths PQ and RS are:

$$2k_1 d\cos\theta - 2\phi_3 - 2\phi_2 = 2\pi N \tag{1.2}$$

ϕ_1 and ϕ_2 are the phase delay from the reflecting interface and given for TE by

$$\phi_{2\perp} = a\tan\left[\frac{\gamma}{\kappa}\right] \quad \phi_{3\perp} = a\tan\left[\frac{\delta}{\kappa}\right] \tag{1.3}$$

where $\gamma \equiv \sqrt{\beta^2 - k_0^2 n_2^2} = \sqrt{\beta^2 - k_2^2}$ and $\delta \equiv \sqrt{\beta^2 - k_3^2}$. The propagation constants are expressed by

$$\begin{cases} \beta = k_1 \sin\theta \\ \kappa = k_1 \cos\theta \end{cases} \qquad \beta = \sqrt{n_1^2 k_0^2 - \kappa^2} \tag{1.4}$$

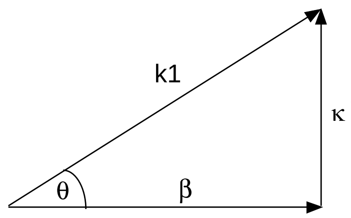

Now we can express the phase-matching Eq. 1.2)) by

$$\kappa d \, \frac{\sqrt{k_0^2 d^2 \left(n_1^2 - n_2^2\right) - \kappa^2 d^2} + \sqrt{k_0^2 d^2 \left(n_1^2 - n_3^2\right) - \kappa^2 d^2}}{(\kappa d)^2 - \sqrt{k_0^2 d^2 \left(n_1^2 - n_2^2\right) - \kappa^2 d^2}\sqrt{k_0^2 d^2 \left(n_1^2 - n_3^2\right) - \kappa^2 d^2}} = \tan(\kappa d) \tag{1.5}$$

The square root term in the left-hand side of the phase-matching equation should be real therefore the following condition should be satisfied

$$k_0^2 d^2 \left(n_1^2 - n_2^2\right) - \kappa^2 d^2 > 0 \Rightarrow k_0 d \sqrt{\left(n_1^2 - n_2^2\right)} > \kappa d \tag{1.6}$$

The upper limit for κd is known as the *normalized frequency* and expressed by

$$\upsilon \equiv \kappa d_{\max} = k_0 d \sqrt{\left(n_1^2 - n_2^2\right)} \tag{1.7}$$

In wavelength we obtain

$$\lambda_c = \frac{2\pi}{\upsilon_c} d \sqrt{\left(n_1^2 - n_2^2\right)} \quad \text{or} \quad \lambda_P^{(m)} \equiv \frac{2\pi}{\beta_m} \tag{1.8}$$

The waveguide operates in single mode for wavelength longer than λ_c. Since $n_1 > n_2 \geq n_3$ eqn.(1.8) holds for n_3. When $n_2 \neq n_3$ there will be a cutoff condition when $\upsilon_c \equiv \kappa d_{\max} = \pi/2$, and addition also satisfied:

$$n_1 > \frac{\beta}{k_0} \geq n_2 \tag{1.9}$$

β / k_0 is a dimensionless value and is a refractive index itself for the plane wave. Therefore it is called the *effective index* and is usually expressed as

$$\mathrm{n}_{\mathrm{eff}} = \frac{\beta}{k_0} = \frac{k_1 \sin\theta_m}{k_0} = n_1 \sin\theta_m \tag{1.10}$$

1.1.2. Rectangular Waveguide

In this section the wave analysis is described for the rectangular waveguide with the method proposed by Mercantili [1].The important assumption of this method is that the electromagnetic field in the shaded area in figure 1.2 can be neglected, since the electromagnetic field of the well-guided mode decays quite rapidly in the cladding region.

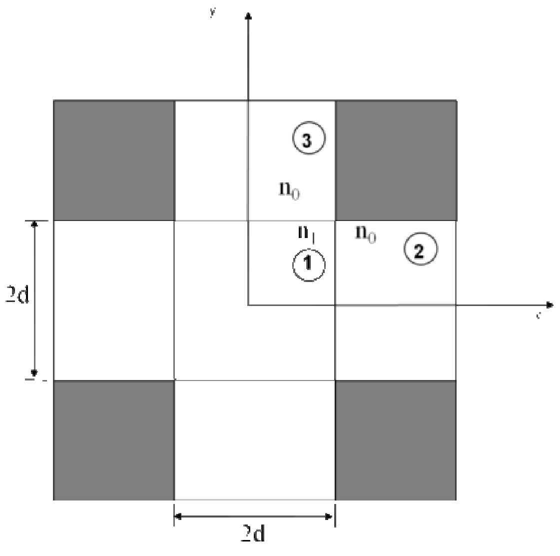

Figure 1.2: Three-dimensional rectangular waveguide.

Taking into account the fact that we treat dielectric optical waveguide, we present the Maxwell's equations for homogeneous and lossless dielectric medium in the terms of electric field E and magnetic field H.

$$\nabla \times \vec{E} = -\mu_0 \frac{\partial \vec{H}}{\partial t} \tag{1.11}$$

$$\nabla \times \vec{H} = \varepsilon_0 n^2 \frac{\partial \vec{E}}{\partial t} \tag{1.12}$$

Where ϵ_o and μ_o denote the permittivity and permeability of the medium respectively.n is the refractive index. We seek wave propagation in the form of

$$\vec{E} = \vec{\mathrm{E}}(\mathrm{x},\mathrm{y})\mathrm{e}^{\mathrm{j}(\omega t - \beta z)} \tag{1.13}$$

$$\vec{H} = \vec{\mathrm{H}}(\mathrm{x},\mathrm{y})\mathrm{e}^{\mathrm{j}(\omega t - \beta z)} \tag{1.14}$$

Substituting Eqs. (1.13) and (1.14) into Eqs. (1.11) and (1.12) the following set of equations are obtained

$$\frac{\partial^2 H_x}{\partial x^2} + \frac{\partial^2 H_x}{\partial y^2} + (k^2 n^2 - \beta^2) H_x = 0$$

$$\begin{cases} H_y = 0 \\ E_x = \dfrac{1}{\omega\varepsilon_0 n^2 \beta} \dfrac{\partial^2 H_x}{\partial x \partial y} \\ E_y = \dfrac{\omega\mu_0}{\beta} H_x - \dfrac{1}{\omega\varepsilon_0 n^2 \beta} \dfrac{\partial^2 H_x}{\partial y^2} \\ E_z = \dfrac{j}{\omega\varepsilon_0 n^2} \dfrac{\partial H_x}{\partial y} \\ H_z = \dfrac{-j}{\beta} \dfrac{\partial H_x}{\partial x} \end{cases}$$

(1.15)

$$\frac{\partial^2 H_y}{\partial x^2} + \frac{\partial^2 H_y}{\partial y^2} + (k^2 n^2 - \beta^2) H_y = 0$$

$$\begin{cases} H_x = 0 \\ E_x = \dfrac{\omega\mu_0}{\beta} H_y + \dfrac{1}{\omega\varepsilon_0 n^2 \beta} \dfrac{\partial^2 H_y}{\partial x^2} \\ E_y = \dfrac{1}{\omega\varepsilon_0 n^2 \beta} \dfrac{\partial^2 H_y}{\partial x \partial y} \\ E_z = \dfrac{-j}{\omega\varepsilon_0 n^2} \dfrac{\partial H_y}{\partial x} \\ H_z = \dfrac{-j}{\beta} \dfrac{\partial H_y}{\partial y} \end{cases}$$

(1.16)

The solution can be express as

$$H_y = \begin{cases} A\cos(k_x x - \phi)\cos(k_y y - \psi) & region\ 1 \\ A\cos(k_x d - \phi)e^{-\gamma_x (x-a)}\cos(k_y y - \psi) & region\ 2 \\ A\cos(k_x x - \phi)e^{-\gamma_y (y-a)}\cos(k_y d - \psi) & region\ 3 \end{cases} \tag{1.17}$$

Where the transverse wave number κ_x , κ_y, γ_x and γ_y and the optical phases ϕ and Ψ are given by

$$\begin{cases} -k_x^2 - k_y^2 + k^2 n_1^2 - \beta^2 = 0 & region\ 1 \\ \gamma_x^2 - k_y^2 + k^2 n_1^2 - \beta^2 = 0 & region\ 2 \\ -k_x^2 + \gamma_y^2 + k^2 n_1^2 - \beta^2 = 0 & region\ 3 \end{cases} \tag{1.18}$$
$$\Rightarrow \beta = \sqrt{k^2 n_1^2 - (k_x^2 + k_y^2)}$$

and

$$\begin{cases} \phi = (p-1)\dfrac{\pi}{2} & (p = 1,2...) \\ \psi = (q-1)\dfrac{\pi}{2} & (q = 1,2...) \end{cases} \tag{1.19}$$

When we apply the boundary conditions for the electric field E_z at x=d and for the magnetic field E^x_{pq} for y=d we obtain the following dispersion equation:

$$k_x a = (p-1)\frac{\pi}{2} + \tan^{-1}\left(\frac{n_1^2 \gamma_x}{n_0^2 k_x}\right) \tag{1.20}$$

$$k_y a = (q-1)\frac{\pi}{2} + \tan^{-1}\left(\frac{\gamma_y}{k_y}\right) \tag{1.21}$$

As we are determining the fields for a symmetrical waveguide, the dispersion equation for E^y_{pq} is give by

$$k_x a = (p-1)\frac{\pi}{2} + \tan^{-1}\left(\frac{\gamma_x}{k_x}\right) \tag{1.22}$$

$$k_y a = (q-1)\frac{\pi}{2} + \tan^{-1}\left(\frac{n_1^2 \gamma_y}{n_0^2 k_y}\right) \tag{1.23}$$

1.2.Nanocrystal background

Our long-term objective is to investigate the utilization of chemically-synthesized Semi-Conductor Nano-Crystals (SC NCs) dispersed in polymer optical waveguides for creating active and/or nonlinear optical devices operating in the near-IR, and to demonstrate that they offer similar — and sometimes unique — functionality to that of the epitaxial approach. The epitaxial growth approach is well understood and developed, and dominates the photonic component marketplace. But the fabrication facilities are costly to install, maintain, and operate, and the production process consists of many time consuming steps, all leading to the high cost of photonic components. The alternative multidisciplinary approach of utilizing colloid chemistry with planar fabrication procedures allows for a novel approach toward realizing simpler integration of NCs into optical devices. The chemical synthesis approach only requires a two step process; the preparation of the colloidal semiconductor nanocrystals followed by the application of a capping or shelling layer that serves to passivate the semiconductor surface states and enable uniform dispersal into the polymer. This synthesis procedure can be performed on bulk quantities, and the NC can be stored until needed for further processing in the colloidal state. Planar waveguide fabrication consists of spin coating, baking, lithography, and etching steps, which are very simple to perform for polymer materials. An additional simplification arises from the fact that the facility that produces the nanocrystals can be disjoint from the optical waveguide fabrication facility, as opposed to the case for semiconductor epitaxial growth facilities. The significance of the composite approach is that the nanocrystals can be synthesized and engineered with desirable optical properties, while the polymer waveguides can be independently optimized for optical fiber mode matching and utilize simplified fabrication. This specific project will promote controlling the orientation of nanocrystals within the polymer matrix, thus expressing the unique features associated with the NC's orientation onto the composite material.

The properties of nanocrystals are governed by their bulk crystalline properties that are altered by their shape and physical confinement, which causes quantization of the energy levels while increasing the effective bandgap. Control over the size and shape of colloidal NCs is accomplished by simple control over the supply of precursors and thermal conditions during the chemical reactions that govern their growth. Further filtering procedure can be applied to narrow the NC's size distribution such that the optical activity matches the wavelength range of interest.

Due to size-controlled spectral tunability and chemical flexibility, semiconductor (SC) colloidal nanocrystals are very attractive for light-interacting applications, including fluorescent tagging [1], light-emitting diodes [3], and lasing [4]. The NCs show high photoluminescence, but limited gain properties due to low absorption cross-section [3], and fast nonradiative carrier recombination due to Auger recombination and abundance of surface states [5]. These shortcomings are dealt by surface passivation of the NCs using chemical ligands (called also "capping"), or growing an external "shell" made of different semiconductor material. The external interface can further serve to allow miscibility of NCs in different materials. The shell can also serve to alter the electronic levels by creating regular (or "Type I") electronic structure, where the electrons and holes are confined in the core, or "Type II" electronic structure, where the holes are confined in the shell. The latter configuration decreases the Auger recombination rate due to charge separation [6]. Growing NC in the shape of nanorods (NRs) is another way to decrease the Auger recombination rate while increasing the optical cross-section, and adding polarization dependence to its optical interactions [7, 8].

Figure 1.3 summarizes the bandgap size of different SC quantum dots (QDs). One can clearly see that some of the materials possess active properties in optical telecommunications wavelength of interest, i.e. InAs, PbS, PbSe, etc. Other NCs are interesting due to their permanent dipole moment (i.e., CdSe) which is amenable to external electric field orientation.

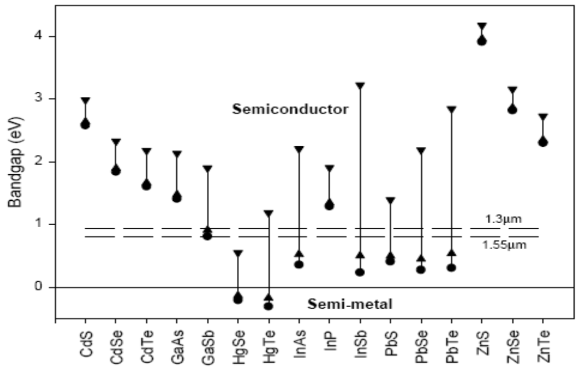

Figure 1.3: Sensitivity of bandgap energies to particle size for a range of semiconductors. Bandgaps are shown for the bulk forms (circles) and at dot radii of 10 nm (up triangles) and 3 nm (down triangles). From Ref. [9].

1.3. Polymers Selection

Choosing a host material for the SC NC suitable for the telecommunications band (normally around 1550 nm, with applications also at 800 and 1300 nm) requires special care, as the host must offer not only miscibility of the NC, but also transparency at the wavelength range, processing at limited temperatures and compatibility with planar fabrication methodologies. NC-host composites have been demonstrated with glasses, sol-gels, and polymers, with glasses requiring elevated temperatures that can ruin organic capping layers. In this work we shall explore polymer hosts, due to their compatibility with NC ligands and simple fabrication requirements. However, many polymers have molecular bonds that result in high absorption in the IR (InfraRed) region due to resonances at these energies (especially the OH and CH bonds)[10,11]. Fluorinated materials have been a subject of research for this reason. Removing hydrogen and replacing it with fluorine in the organic network negates absorption due to the C-H bonds that have strong absorption in the visible and near infrared regions which is where most communication systems operate. Absorption due to C-F bonds occurs at longer wavelengths compared to their C-H counterparts [1]. Flouropolymers are well suited for waveguiding IR light as they exhibit very low absorption (<0.15dB/cm) over the range of 400-1600nm, offer high temperature stability and long durability, can be patterned using standard spin-coating, lithography and etching procedures, and have been combined with NCs to form a composite [12]. I will focus on device construction in Per-Flourinated Cyclo-Butane (PFCB) polymer as core material.

For the cladding material I choose Cytop™ with refractive index of 1.34 which shows excellent clarity and solubility to fluorinated solvents[13], can be patterned using standard spin-coating, lithography and etching procedures in addition has exhibit excellent transparency over a wide range of wavelengths including IR region [13].

This polymer combination allows us to create high index contrast Δn of ~10% which allows highly confined optical mode operation.

2. Single-Mode Waveguide Parameters Selections

2.1. Waveguide Design Requirements

This chapter presents the design and analysis of a high index contrast (HIC) single-mode waveguide in highly confined geometries construction in PFCB polymer using Cytop as the outer cladding material. In figure 2.1 we can see a schematic design of triple-layer stack geometry WG where h is the height and w is the width of the PFCB core and d is the Cytop layer thickness between the silicon substrate and the PFCB core. In order to cope with the fabrication variation we design devices with different width and dimensions such as ring resonators. This WG design and analysis is partially based on previous work [14] done in Dan Marom group.

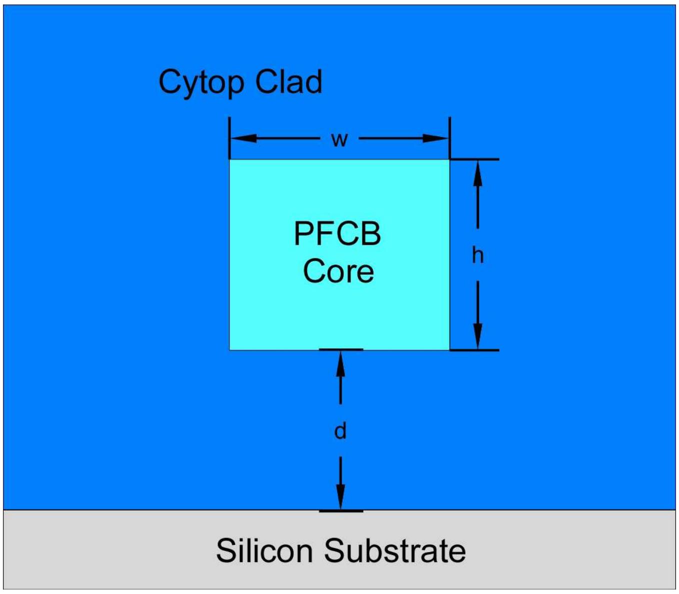

Figure 2.1: Schematic design of a triple-layer stack geometry WG.

2.2. Waveguide Core Width and Height Selection

The single mode criteria can be found with numerical techniques by extrapolation of the effective index associated with the fundamental mode as a function of waveguide dimensions and finding the intersection of this with the cladding index. This is shown in figure 2.2. From figure 2.2 we conclude the cut-off dimensions criteria for single mode is 1.6μm for a square core, therefore 1.5μm waveguide width and height was selected. We choose a square waveguide (w=d) geometry to overcome polarization effects that occur when the waveguide core is not a symmetrical one.

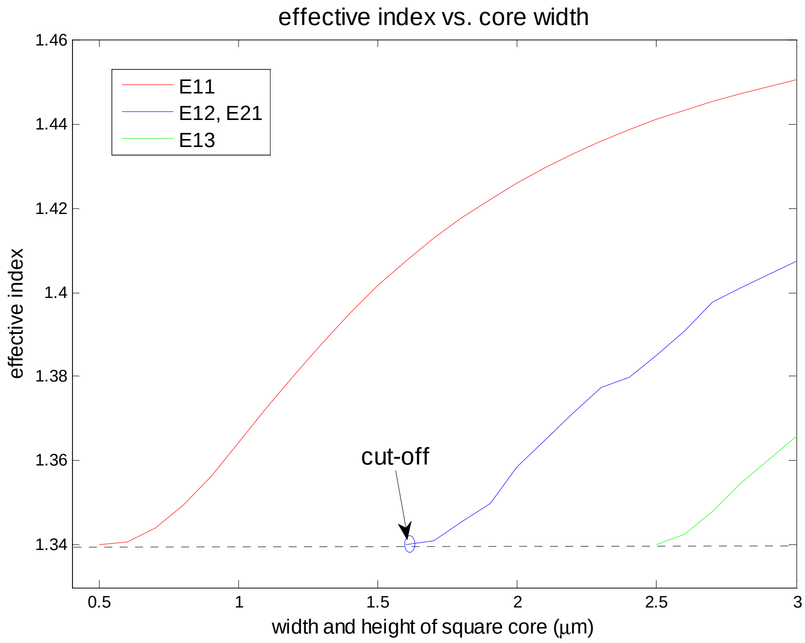

Figure 2.2: Shows the approximate cut-off of the first fundamental E_{11}^{x} mode of a PFCB - Cytop waveguide with a core having a square cross-section. This defines the single mode criteria for high-index waveguides.

2.3. Polarization

2.3.1. Birefringence

When a waveguide doesn't have a symmetrical geometry it will have different propagation constants for different polarizations, as shown in figure 2.3. Notice in figure 2.3 the effective indexes of the two different polarizations cross when the width of the waveguide is 1.5μm (the waveguide is symmetric).We define the birefringence as

$$\Delta n = (n_{TEeff} - n_{TMeff}) \tag{2.1}$$

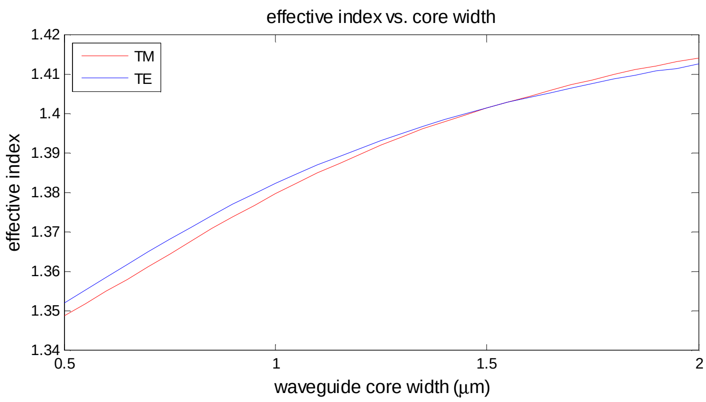

Figure 2.3: The calculated effective index of 1.5μm PFCB core thickness as a function of waveguide width. Note the geometrically induced birefringence for waveguides not having a symmetric core.

2.3.2. Effective Group Index

The effective index does not just vary as a function of waveguide dimensions; it also varies with the wavelength. Longer wavelengths tend to be less confined and have lower effective indexes. The geometric origins of this variation associated with the waveguide cross-section can be explored by assuming that the refractive index of the materials doesn't change significantly over the wavelength range being considered.

The group velocity of a guided mode υ_g is given by [1]:

$$\upsilon_g = \frac{1}{\frac{\partial \beta}{\partial \omega}} \tag{2.2}$$

where β is the propagation constant and ω is the angular frequency. The angular frequency is related to the wavelength through the expression $\omega = 2\pi \frac{c}{\lambda}$, and the propagation constant is related to the effective index through $\beta = n_{eff} \frac{2\pi}{\lambda}$.The chain rule can be applied and an expression for the group velocity derived.

$$\upsilon_g = \frac{c}{n_{eff} - \lambda \frac{\partial n_{eff}}{\partial \lambda}} \stackrel{\Delta}{=} \frac{c}{n_g} \tag{2.3}$$

Where it has been assumed that the effective index is a function of the wavelength, and n_g is the effective group index associated with a mode. Figure 2.4 shows the effective group index as a function of wavelength. Two cases are shown, one that corresponds to a waveguide with a square core (1.5µm×1.5µm) and one that corresponds to a waveguide with rectangular core dimensions of 0.85µm×1.5µm. In the latter case, the polarization modes are split.

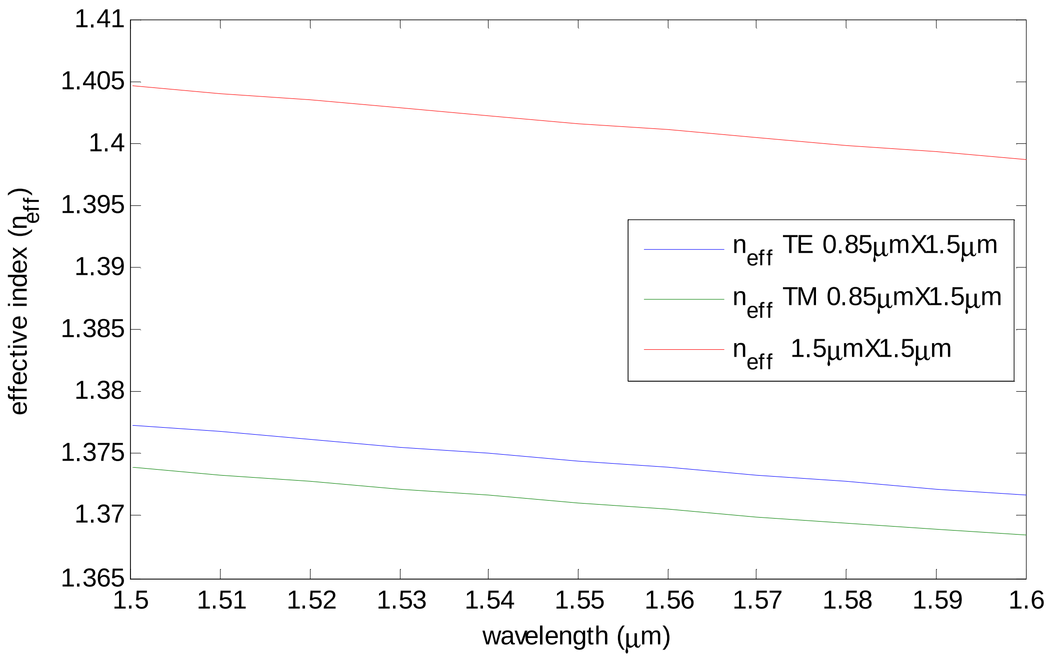

Figure 2.4: The calculated effective group index of high-index contrast waveguides, based solely on waveguide geometry, with two different cross-sectional dimensions: 1.5μm×1.5μm, referred to as symmetric; and 0.85μm×1.5μm referred to by the width, 0.85μm. Note that the polarizations are degenerate in the symmetric case.

The different group velocities for the TE and TM polarizations lead to polarization mode dispersion (PMD). Figure 2.4 shows the different group indexes associated with the polarizations as a function of wavelength for two waveguides - one that is symmetric where the group index is degenerate with respect to the polarization; and one that is asymmetric. This is, however, not a broad-band effect and generally speaking the more asymmetric the waveguide becomes, the more polarization mode dispersion there will be. From figure 2.4 I calculated that for waveguide with core dimensions of 1.5μmX1.5μm at 1.55μm wavelength the effective group index is 1.49.

2.4. Mode Profile

2.4.1. Mode Simulation

In order to achieve a single mode waveguide with good mode confinement, the effective index of the waveguide should be above Cytop (n=1.34). The mode profile simulations have been performed on Comsol 4, a 2-D mode solving simulation program. Figure 2.5 shows the simulated results for square waveguide, where the mode intensity profile has been calculated (w=d=1.5μm) for TE incident wave (the TM intensity mode profile is identical as explained in **2.3.1**). Figure 2.6 shows the simulated results for rectangular waveguide with core dimensions of 0.85μm×1.5μm, where the mode intensity profile has been calculated for both TE and TM incident waves.

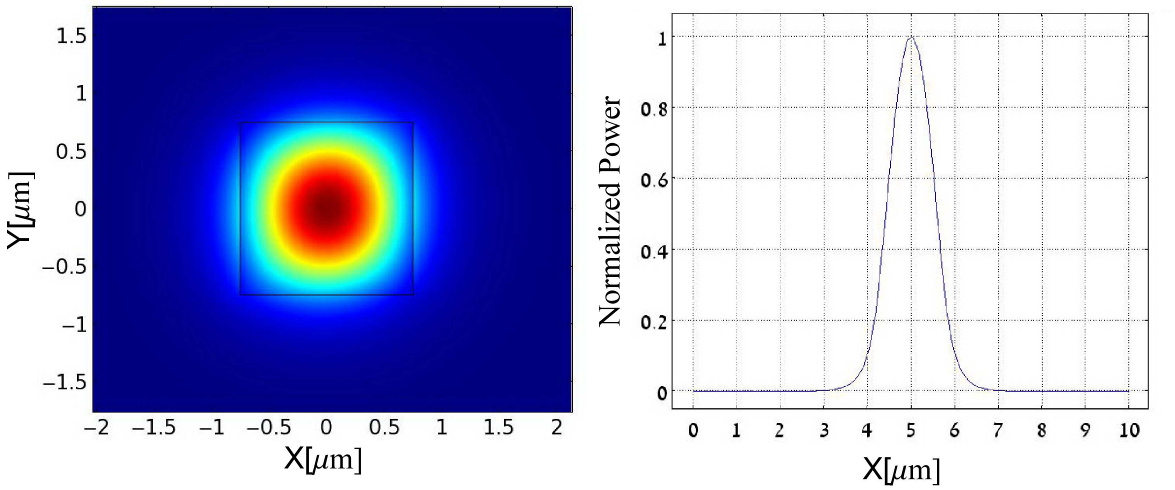

Figure 2.5: Simulated TE intensity mode profile result for 1.5μm×1.5μm square waveguide with a 1.88μm waist.

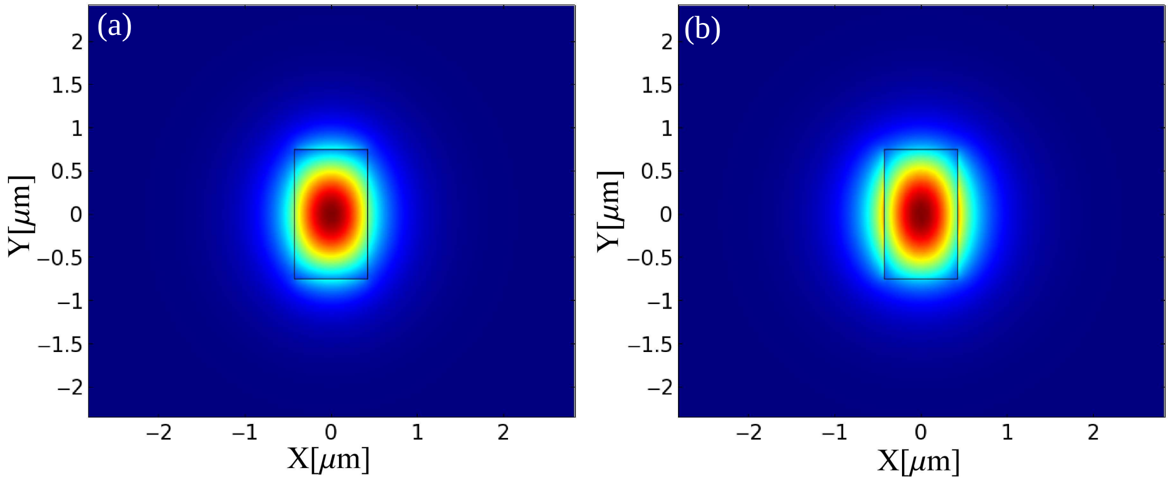

Figure 2.6: Simulated TE(a) and TM(b) intensity mode profile results for 0.85μmX1.5μm rectangular waveguide with a 1.906μm×2.06μm waist.

2.4.2. Modal Confinement

The modal confinement is defined as the fraction of the power in a guided mode traveling along a waveguide that is confined to the core region. It is related to the effective index and for a given core and cladding materials, it is expected that a higher effective index generally translates into a higher modal confinement. The fundamental mode tends to be the most confined just as it tends to have the highest effective index. The fundamental mode's fractional power confinement of a 1.5μm×1.5μm waveguide core at a wavelength of 1550nm is calculated by Eq. 2.4 [1] which gives approximately Γ=0.56 and Γ=0.47 for 0.85μm×1.5μm waveguide core (as calculated with Comsol 4 software).

$$\Gamma = \frac{P_{core}}{P_{core} + P_{clad}} \tag{2.4}$$

Related to the modal confinement is the spot size of the propagating field and the optical intensity. When the modes are highly confined in a small core the optical intensity is high. The spot size (beam radius) of a 1.5μm×1.5μm waveguide core at a wavelength of 1550nm is approximately 1.88μm as shown in figure 2.5(e^{-2} waist of the power density), when making a Gaussian approximation (reference for Gaussian approximation [15]). This means the optical intensity for 0dBm is approximately [1]:

$$I = \frac{P}{\pi W^2} = 9\times 10^3 \frac{W}{cm^2} \tag{2.5}$$

2.5. Substrate Leakage

Substrate leakage happens when the low index under-cladding layer is too thin to provide sufficient optical insulation between the high index Si substrate, as shown in figure 2.6a for 0.35μm Cytop under-cladding layer. This can be prevented easily with a careful designed substrate separation as shown in figure 2.7. For 3.5μm Cytop under-cladding layer the substrate leakage is negligible as shown in figure 2.6b.

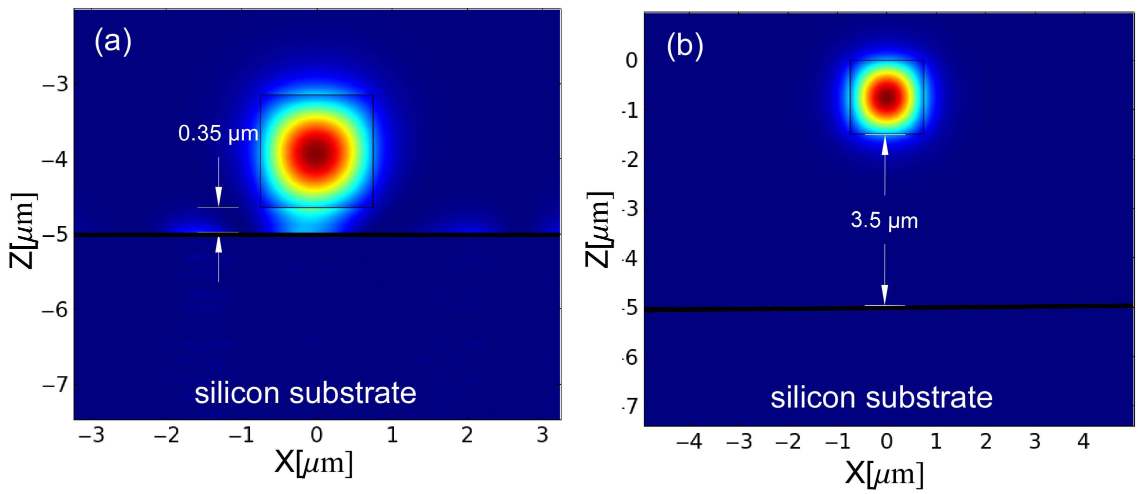

Figure 2.6: Comsol mode solver leakage mode solution examples. (a) TM intensity mode profile for 1.5μm×1.5μm square waveguide with 0.35μm Cytop under-clad separation. (b) TM intensity mode profile for 1.5μm×1.5μm square waveguide with 3.5μm Cytop under-clad separation.

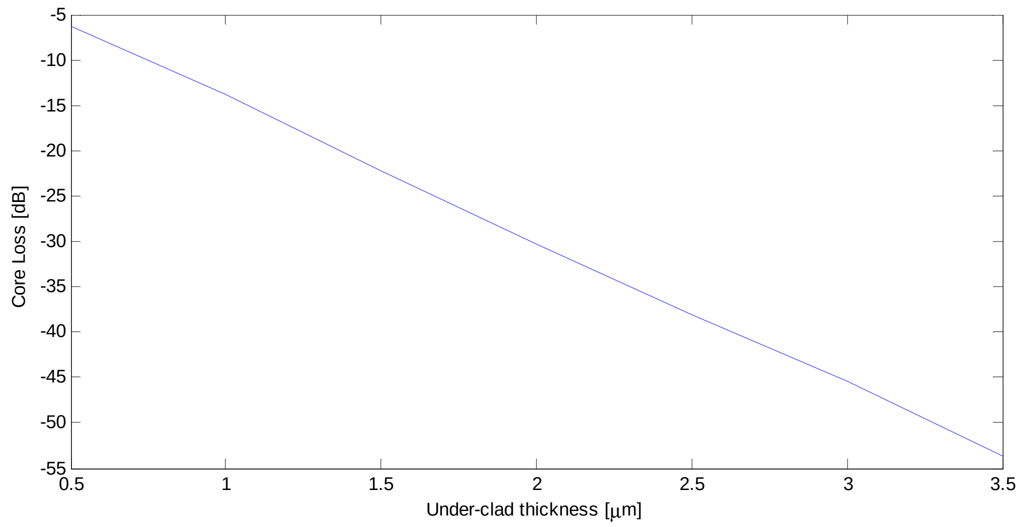

Figure 2.7: The substrate leakage loss vs. under-clad thickness computed by comsol mode solving simulation program for 0dBm input power.

2.6. Mask Design

The first step, prior fabrication, is to design a layout for the signal lithography mask required. The mask used in this process defines the shape and location of each waveguide structure in the x-z plane of the die. In order to characterize the waveguide propagation and bending loss waveguides with different parameters have been designed.

2.6.1. Propagation Loss

The presence of optical loss not only provides unwanted signal attenuation while traveling inside the waveguides, but also affects the performance of many waveguide-based optical devices such as couplers. Compared to optical fused silica fibers which only has a fraction of dB per kilometer, high transmission loss associated with polymeric waveguides is due to high index contrast in these waveguides and their planar geometry. The mechanisms that can contribute to optical loss in waveguides include Raleigh scattering [16], which is caused by fluctuations in the refractive index, which from previous work expected to be 0.29dB/cm at 1550nm[10]; and irregularities at the interface between the core and cladding materials. Irregularities at the interface between the core and cladding are usually more pronounced on the sides of the waveguides that are defined by etching. The sidewalls of the waveguide tend to be rougher because they are defined through a lithographic process from a mask which has a certain inherent roughness, and the transfer of the pattern goes through exposure, development, and etching.

The simple analytical model proposed by Tien [17] shows that propagation loss α due to sidewall roughness is defined as:

$$\alpha = \frac{4\sigma^2 h^2}{\beta\left(r + 2/p\right)} = \frac{\sigma^2 k_0^2 h}{\beta} \cdot \frac{E_s^2}{\int E^2 dx} \cdot \Delta n^2 \tag{2.6}$$

where σ is the interface roughness, *t* is the waveguide thickness,k_0 is the free space,β is modal propagation constant, Δn the difference between the refractive indices of the core and cladding, while *h* and *p* are the transverse propagation constants in the core and cladding, respectively. It is seen that loss is proportional to $E_s^2 / E^2 dx$, the normalized electric field intensity at the core/cladding interface and to the square of interface roughness σ.

Generally, the combination of waveguide propagation loss and fiber to waveguide coupling loss is called the insertion loss which represents the total attenuation of the system [dB]:

$$\alpha_i = \alpha_c + \alpha_p \cdot L \tag{2.7}$$

where α_ι is the total insertion loss [dB], α_c is the total coupling loss [dB], α_p is the waveguide propagation loss coefficient [dB/cm], and L is the waveguide length [cm].

The waveguide transmission loss coefficient can be accurately measured by the following method: Fabry-Perot resonance technique [18], "cutback" method [19] and Ring resonator resonance technique [20].

2.6.1.1. Fabry-Perot Resonance Technique

A common method to measure optical waveguide is to launch signal from optical fiber into waveguide from the input port on one edge of the chip and pick up output signal from the output port on the other edge. In order to reduce scattering during fiber to waveguide coupling, chip edge where waveguides are exposed are polished to obtain smooth facets. This creates a resonance cavity along the waveguide between the two highly reflective facets. Using Fresnel equation and assuming normal incidence at parallel waveguide facets we receive:

$$R = \left(\frac{n_{incident} - n_{eff}}{n_{incident} + n_{eff}}\right)^2 \tag{2.8}$$

Where R is the reflectance; $n_{incident}$ is the refractive index of air.

Each set of cavity length and effective index has a characteristic feature created by interference effect due to the phase difference for different path length. The constructive interference satisfies:

$$L = m \cdot \frac{\lambda}{n_{eff}} \tag{2.9}$$

where L is the length of the waveguide; m is an integer number and represents the number of round-trip that light has traveled in between the two facets. The waveguide loss can be calculated from:

$$\alpha_p = \frac{1}{L} \ln \left(R \cdot \frac{1+\sqrt{\frac{P_{\min}}{P_{\max}}}}{1-\sqrt{\frac{P_{\min}}{P_{\max}}}} \right) \tag{2.10}$$

Where $P_{\max}$ is the maximum transmitted power and $P_{\min}$ the minimum transmitted power.

One advantage of this method is that it is independent on the value of the coupling losses. The drawback of the Fabry-Perot resonance technique is that the actual reflectance, R, always deviates from ideal case due to tilted facet, roughness, and tilted incident angle.

2.6.1.2. "Cutback" Method

From Equation 2.7, we know that insertion loss is dependent on waveguide length. If we keep the coupling loss constant then the total loss will become a linear function of waveguide length. In figure 2.8 we can see lithography mask layout with waveguide length varying from 26408μm to 62408μm. The bend angles at the "paperclip" shapes are equal so that their contribution can be cancelled.

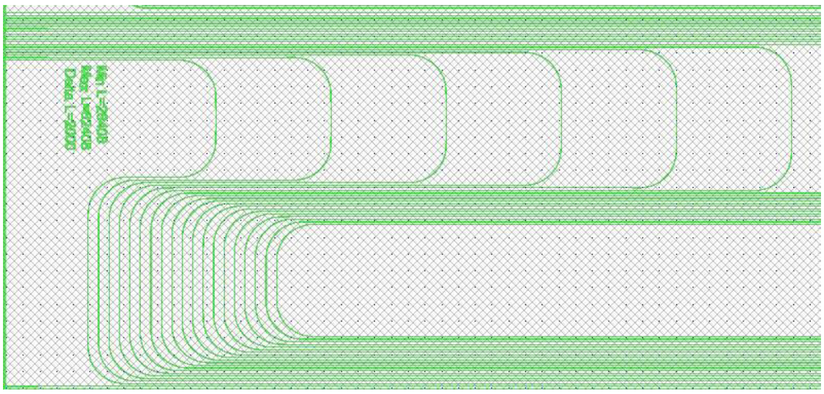

Figure 2.8: Lithography mask layout of propagation losses array.

2.6.1.3. Ring Resonator Resonance Technique

Ring resonator (or racetrack resonators) are not only photonic devices for filter, but also useful to derive waveguide propagation loss coefficient. Figure 2.9 shows schematically a ring resonator with a single directional coupler (DC), and gives the notation used. For the coupler in figure 2.9b, the fields b and b' at the outputs are related to the fields a and a' at the inputs by self-coupling coefficients t_c and t'_c, and the cross-coupling coefficients κ_c and κ'_c, according to Eqs. (2.11) and (2.12):

$$b = t_c a + \kappa_c^{'} a^{'} \quad (2.11)$$

$$b^{'} = t_c^{'} a^{'} + \kappa_c a \quad (2.12)$$

$$a^{'} = t_r^{'} b^{'} \quad (2.13)$$

Substituting Eq. (2.13) into Eq. (2.12) gives Eq. (2.14):

$$b = \left(t_c - \left(t_c t_c^{'} - \kappa_c \kappa_c^{'}\right) t_r^{'}\right) a \quad (2.14)$$

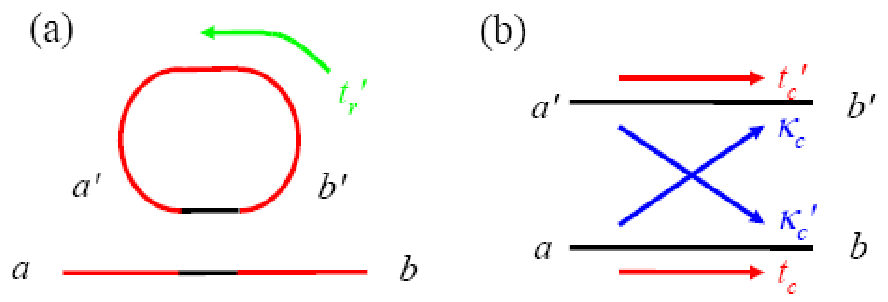

Figure 2.9: Ring resonator with a directional coupler (DC): (a) schematic of the DC-coupled resonator and (b) expanded view of the coupler, showing the notation used in the text for the fields (a, b, a' and b'), the self-coupling coefficients t_c and t_c', the cross-coupling coefficients κ_c and κ_c', and the transmission t_r' around the ring [20].

Since energy is conserved, the following Eq. (2.15) holds:

$$|b|^2 + \left|b^{'}\right|^2 = \alpha_c^2 |a|^2 + \alpha_c^{'2} \left|a^{'}\right|^2 \quad (2.15)$$

Substituting b and b' from Eq. (2.12) and Eq. (2.13) into Eq. (2.16) gives the following relations, Eqs. (2.16), (2.17) and (2.18):

$$|t_c|^2 + |\kappa_c|^2 = \alpha_c^2 \quad (2.16)$$

$$\left|t_c^{'}\right|^2 + \left|\kappa_c^{'}\right|^2 = \alpha_c^{'2} \quad (2.17)$$

$$t_c^{*} \kappa_c^{'} + \kappa_c^{*} t_c^{'} = 0 \quad (2.18)$$

Eqs. (2.17) and (2.18) lead to the following relation Eq. (2.19), which can be used in Eq. (2.14):

$$t_c t_c^{'} - \kappa_c \kappa_c^{'} = \left(t_c^{'} t_c^{'*} + \kappa_c^{'} \kappa_c^{'*}\right) \frac{t_c}{t_c^{'*}} = \alpha_c^{'2} \frac{t_c}{t_c^{'*}} \quad (2.19)$$

To simplify the final result, we introduce the phases $\phi_r^{'}$ and $\phi_c^{'}$ through Eqs. (2.20) and (2.21):

$$t_r^{'} = \left|t_r^{'}\right| e^{i\phi_r^{'}} \quad (2.20)$$

$$t_c^{'} = \left|t_c^{'}\right| e^{i\phi_c^{'}} \quad (2.21)$$

and define the following coefficients in Eqs. (2.22), (2.23), (2.24), and (2.25):

$$\kappa \equiv \left|\kappa_c^{'}\right| / \alpha_c^{'} \tag{2.22}$$

$$t \equiv \left|t_c^{'}\right| / \alpha_c^{'} \tag{2.23}$$

$$\alpha \equiv \left|t_r^{'}\right| \alpha_c^{'} \tag{2.24}$$

$$\phi \equiv \phi_c^{'} + \phi_r^{'} \tag{2.25}$$

Then Eq. (2.14) can be rewritten as Eq. (2.26):

$$\frac{b}{a} = \left(\frac{t - \alpha e^{i\phi}}{1 - \alpha t e^{i\phi}}\right) \frac{t_c}{t_c^{'*}} \alpha_c^{'} e^{-i\phi_c^{'}} \tag{2.26}$$

Taking the absolute square of Eq. (2.26) gives Eq. (2.27):

$$T \equiv \left|\frac{b}{a}\right| = \left|\frac{t_c}{t_c^{'*}}\right|^2 \alpha_c^{'2} \left(\frac{t^2 + \alpha^2 - 2\alpha t \cos\phi}{1 + \alpha^2 t^2 - 2\alpha t \cos\phi}\right) = \left|\frac{t_c}{t_c^{'*}}\right|^2 \alpha_c^{'2} \gamma \tag{2.27}$$

where the factor γ is defined as Eq. (2.28):

$$\gamma = \left(\frac{t^2 + \alpha^2 - 2\alpha t \cos\phi}{1 + \alpha^2 t^2 - 2\alpha t \cos\phi}\right) \tag{2.28}$$

The factor γ determines the shape of the resonances [21]; the other factors in Eq. (2.27) vary more slowly with wavelength. The coefficients α and t can be related to the width and depth of the resonances [22]. Let $\Delta\lambda_{FWHM}$ be the full width at half maximum of a given resonance, and $\Delta\lambda_{FSR}$ be the free spectral range. The finesse F is defined by Eq. (2.29)

$$\gamma \equiv \Delta\lambda_{FSR} / \Delta_{\lambda FWHM} \tag{2.29}$$

and the extinction ratio is defined by Eq. (2.30)

$$\varepsilon \equiv T_{\max} / T_{\min} \tag{2.30}$$

Then the following relations Eqs. (2.31) and (2.32) follow from Eq. (2.28) for γ:

$$\varepsilon = \left[\frac{(\alpha + t)(1 - \alpha t)}{(\alpha - t)(1 + \alpha t)}\right]^2 \tag{2.31}$$

$$\cos(\pi / \gamma) = \frac{2\alpha t}{1 + \alpha^2 t^2} \tag{2.32}$$

Equation 2.32 can be solved for the product αt, and that result can be substituted into Eq. (2.31). The result is a quadratic equation that yields α and t as the two roots. The result can be written in terms of the following two quantities A and B, defined by Eqs. (2.33) and (2.34):

$$A \equiv \frac{\cos(\pi / \gamma)}{1 + \sin(\pi / \gamma)} \tag{2.33}$$

$$B \equiv 1 - \left[\frac{1-\cos(\pi/\gamma)}{1+\cos(\pi/\gamma)} \right] \frac{1}{\varepsilon} \tag{2.34}$$

In terms of these, α and t are given by Eq. (2.35):

$$(\alpha, t) = \left(\frac{A}{B} \right)^{1/2} \pm \left(\frac{A}{B} - A \right)^{1/2} \tag{2.35}$$

In a ring with a directional coupler, t varies approximately sinusoidally with wavelength [23]. On the other hand, α is not expected to depend this strongly on λ when the bending losses are small. Alternatively, t and α could be distinguished by their dependence on device geometry, if different geometries are available. For example, keeping the same coupler geometry but increasing the radius of the ring will leave t unchanged (to within tolerances in the fabrication) but will change α. For small rings, when bending losses dominate, α will decrease as the ring is made smaller. For large rings, where propagation losses dominate, α will decrease as the ring is made larger. Figure 2.10 shows the lithography mask layout of an array of racetrack resonator with different radius and directional coupler spacing.

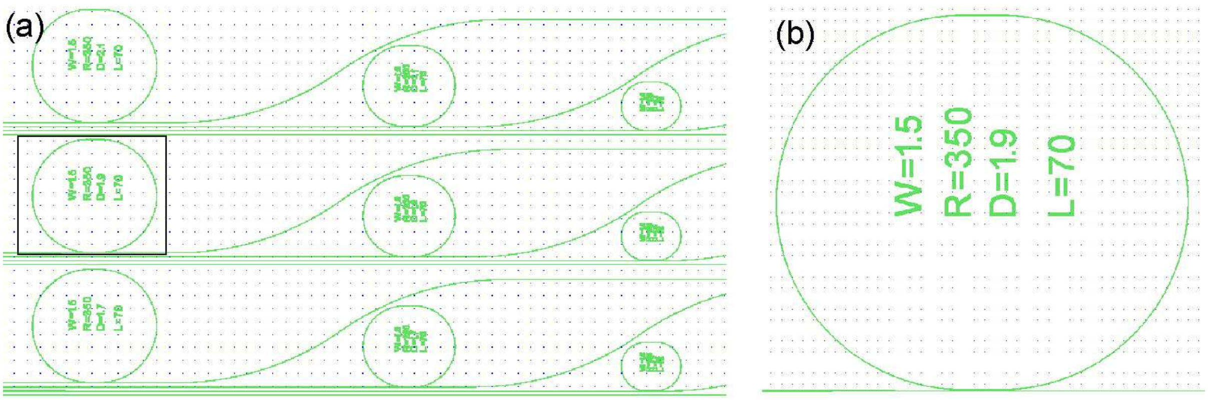

Figure 2.10: (a) Mask layout of racetrack resonators of an array of racetrack resonator with different radiuses and directional coupler spacing. (b) Racetrack resonator with 350μm Radius, 70μm coupling region and 1.9μm coupler spacing.

In order to extract the losses from the loss factor I used the resonance response from ref. [24]:

$$T = \frac{(\lambda - \lambda_0)^2 + \left(\frac{FSR}{4\pi} \right)^2 \left(\alpha'^2 - t'^2 \right)^2}{(\lambda - \lambda_0)^2 + \left(\frac{FSR}{4\pi} \right)^2 \left(\alpha'^2 + t'^2 \right)^2} \tag{2.36}$$

I can distinguish between the coefficients α' and t' using the method described before.

The propagation/bend loss in a round trip is calculated by:

$$-10\times\log_{10}\left(1-\alpha'^{2}\right)dB/round-trip \tag{2.37}$$

The propagation/bend loss in a 90^0 bend is calculated by:

$$-2.5\times\log_{10}\left(1-\alpha'^{2}\right)dB/90^{0} \tag{2.38}$$

2.6.2. Radiation Loss in Bent Waveguides

A curved waveguide results in power attenuation due to the leakage of light around the bend [25]. It is a fundamental issue when designing any type of integrated optical structure. The physical mechanism responsible for bend loss is described by a simple model [25]. An analysis by a conformal transformation, discussed, represents the refractive index in polar coordinates and their transformation into Cartesian coordinate $x = R_t \ln(r / R_t)$ is

$$\tilde{n}(x) = n\left(R_t \exp\left(x/R_t\right)\right)\exp\left(x/R_t\right) \tag{2.39}$$

Where R_t can be chosen arbitrarily. The transformed index profile is shown in figure 2.11 for a curved slab guide with equal to the radius of the outer wall. It indicates the exponential increase of the cladding index as the distance from the center of curvature increases.

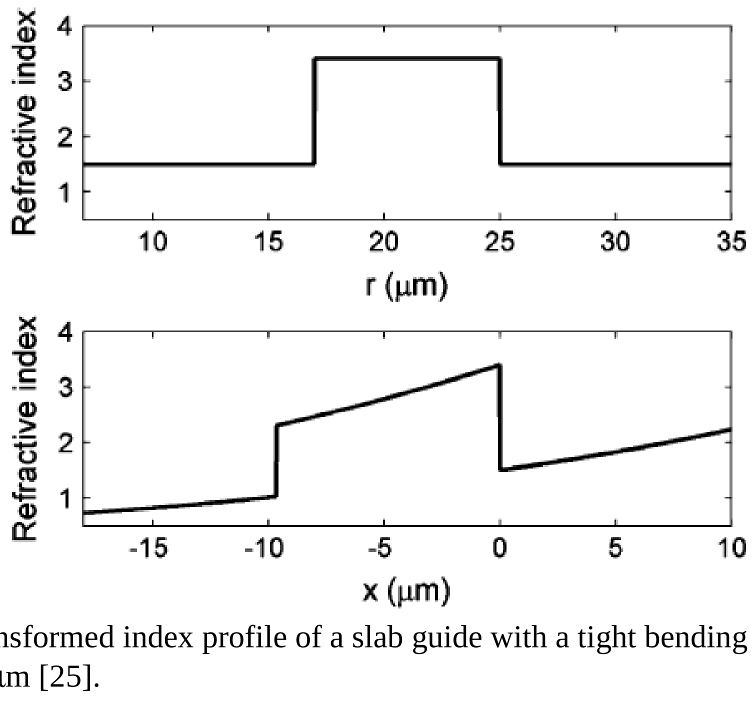

Figure 2.11: Transformed index profile of a slab guide with a tight bending radius at the outer wall of 25 µm [25].

A second effect is a shift of the mode power from the center of bend as a centrifugal force. Figure 2.12 shows a simulation for a bent fiber [25]. This shift, if not taken into account, can lead to a mismatch when the guided mode is coupled in to a straight waveguide or to a bends with a different curvature. To overcome this effect, the use of an offsets is suggested, to best match the mode patterns of coupled dissimilar guides.

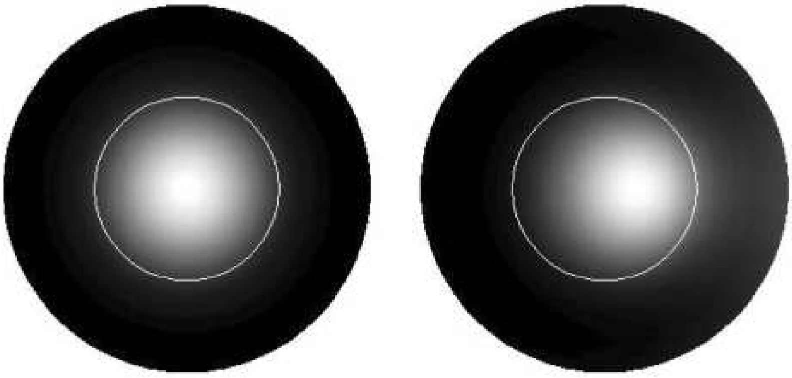

Figure 2.12: Outward shift of the modal field in a bent fiber for R = ∞, left, and R = 1 cm, right [25].

A simple scheme to numerically predict the attenuation of the propagating power in curved waveguides formed by a curved strip of width w and a refractive index n, surrounded by index n-Δn was developed by Dragone [26].An optimization of the overlapping integral between the straight waveguide and the electric fields in the bend, determines the propagation constant

$$\varepsilon_{\infty} \simeq \frac{2}{\sqrt{\left(\frac{2\Delta n}{n}\right)}} \exp\left[-\frac{4}{3}\left(Z^{2} - 2.388 + b\right)^{3/2}\right] \tag{2.39}$$

Where

$$Z = \left(\frac{2\Delta n}{n}\right)^{1/2} \left(\frac{k_0 R}{2}\right)^{1/3} \tag{2.40}$$

$$b = \frac{1}{Z}\left(1 + \frac{0.65}{Z^{2}}\right) \tag{2.41}$$

In figure 2.13 we can see the bend loss as calculated from (2.40) and (2.41) for 90^{o} curvature. Two cases are shown, one that corresponds to a waveguide with a square core (1.5μmX1.5μm) and one that corresponds to a waveguide with rectangular core dimensions of 0.85μmX1.5μm.We can see that loss for square waveguide (1.5μmX1.5μm) are negligible for bends that are higher than 120μm, and for rectangular waveguide (0.85μmX1.5μm) for bends that are higher than 240μm.Clearly, the bend loss is very sensitive to waveguide width therefore lower losses for wider waveguides.

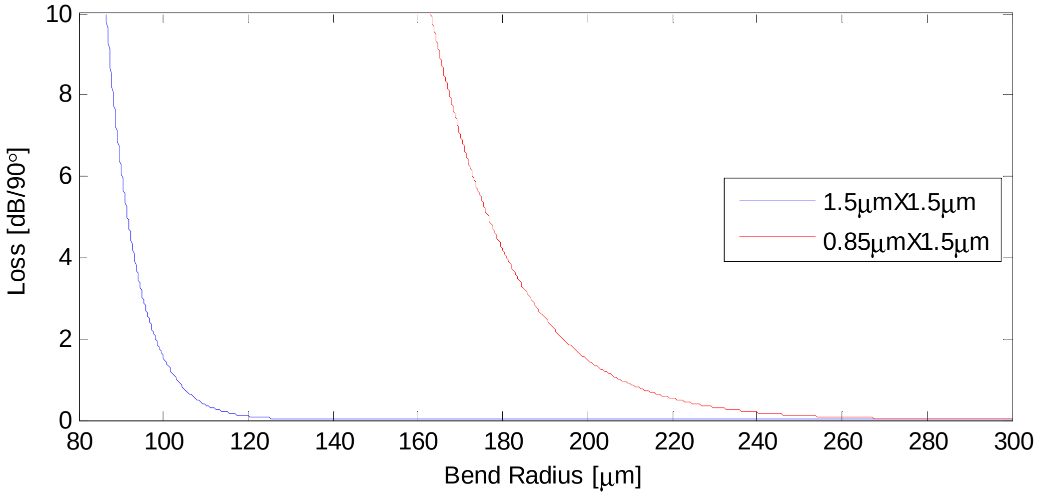

Figure 2.13: Bend loss for 90^{o} curvature waveguide with a square core (1.5μmX1.5μm) and rectangular core (0.85μmX1.5μm).

To characterize bend losses, an array of waveguides were designed, the array includes a varying number of 90^{o} curvatures with different radiuses, all with bends width of 2.5μm. After etch bend a taper narrowed the waveguide into a relaxation straight of the designated waveguide width of a 1.5μm. This was done to let the fundamental mode develop back. The Lithography mask layout of Bend losses array is presented in figure 2.14.Furthermore, a characterization of the bend loss can be provided by a ring resonator as it was explain in **2.6.1.3**.

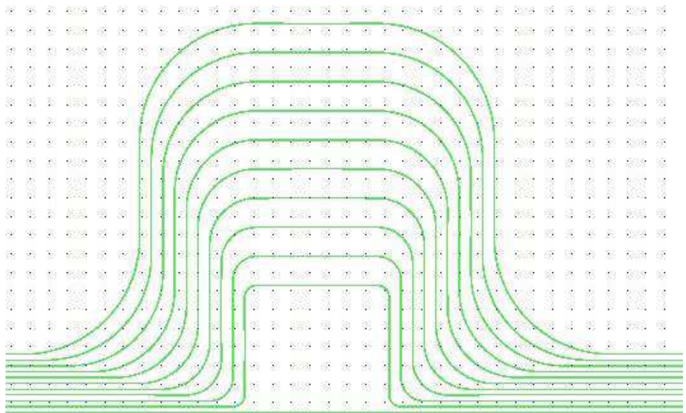

Figure 2.14: Lithography mask layout of Bend losses array with radius bend varying from 50μm to 500μm.

2.6.3. External Coupling

In order to coupled light beam into the waveguide input and output we used commercial lensed fiber with a beam spot size of 2.5μm. Since our waveguide core dimensions are 1.5μmX1.5μm we need the use a taper. To achieve the best coupling efficiencies and mode matching abilities in a taper it is necessary to design a taper that will insert the required mode in to the optical waveguide device by designing a moderate slope taper it is possible to avoid neighboring modes [27]. The taper parameters were calculated using [27] which gave taper width of 3μm and taper length of 150μm as shown in figure 2.15. We design the taper only in the planer dimensions for fabrication reasons. In figure 2.16 we can see a CCD image of coupled light into the fabricated waveguide.

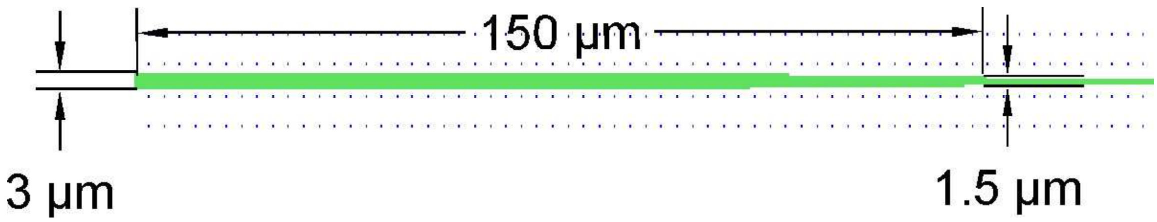

Figure 2.15: Taper mask image with width input of 3μm and length of 150μm.

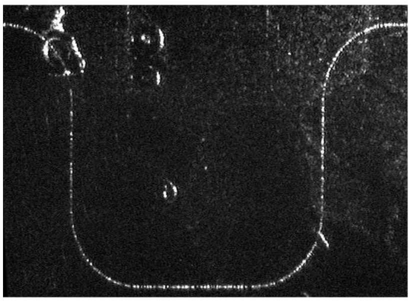

Figure 2.16: CCD image of a coupled light in the waveguide with dimensions of 1.5μm X1.2μm.

3. Waveguide Fabrication

3.1. General Description

The main objective of this work is to develop fabrication process of a waveguide structures with a PFCB polymer as core and Cytop polymer as cladding. . The device structure is shown schematically in figure 3.1.

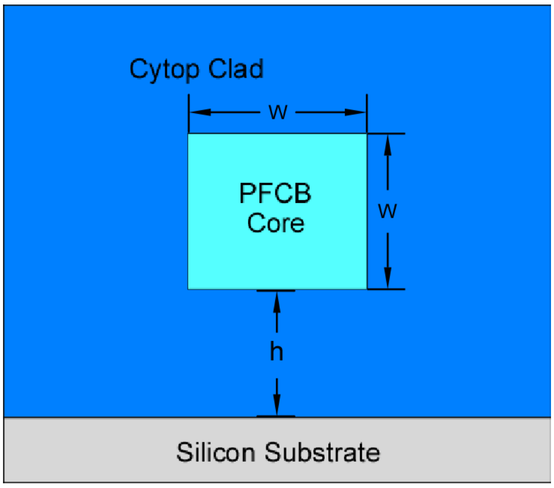

Figure 3.1: Device structure

The developed process flow proved more challenging than expected, due to Cytop's material properties (hydrophobic), {Cytop© is an amorphous, soluble perfluoropolymer produced by Asahi Glass Company having properties of fluorinated polymers including optical transparency and chemical resistance.}And from stress in the PFCB-Cytop films resulting from CTE mismatch with silicon substrate. However, the process is now completely stabilized and reproducible, made possible by introducing nanometric chemical vapor deposition of oxide at low temperatures.

3.2. Process Development

3.2.1. Cytop Adhesion to Silicon

We begin with a polished Silicon wafer that is first treated with Silane coupling agent due to Cytop A grade poor adhesion to silicon substrate. In order to apply the Silane to the wafer, it was slightly agitated in a Silane environment for 5 minutes and then was placed on a hot plate set to 180^0 for duration of 30 minutes.

3.2.2. Cytop Under-Clad

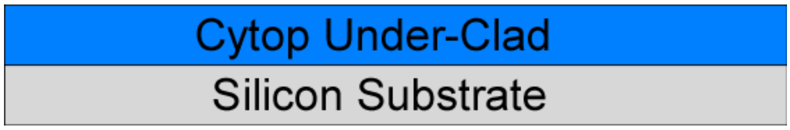

A 3.5 μm thick under-clad layer of Cytop was necessary in order to prevent coupling between the waveguide core and silicon substrate due to the presents of the high refractive index of silicon. The Cytop was spun coated in two steps: The first was in 600 rpm for duration of 7 second in a ramp level 3 in order to spread the Cytop on the wafer, the second was in 1000 rpm for duration of 30 second in a ramp level 3 to achieve the 3.5um desire Cytop layer. Then the wafer was cured in an oven set to 120^0 for duration of 4 hours.

3.2.3. PFCB Adhesion to Cytop

Cytop is an amorphous fluorocarbon polymer as such it is hydrophobic Teflon-like film. A thin film of 30nm Oxide layer was deposited with CVD (chemical vapor deposition) in a temperature of 40^0 in a rate of 10nm/min for duration of 3 minute with 2 mtorr chamber pressure and 13 sccm N_2O and 4 sccm SiH_4 flow rates. This process is necessary to help the next polymer spin coat adhesion to succeed.

3.2.4. PFCB Core Spin Coating

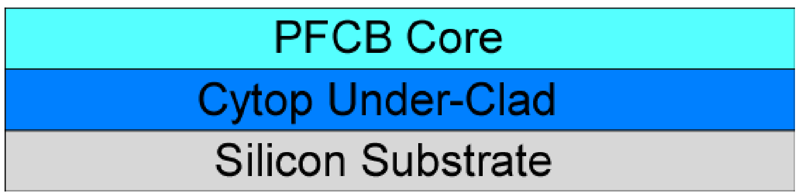

The PFCB polymer was chosen as the core, it was spun coated in 4800 rpm for duration of 45 second to achieve 1.5 μm layer and then cured in a N_2 environment in an oven set to 120^0 for duration of 16 hours. As PFCB is teflon-like film a 10 seconds O_2 plasma etching surface treatment is needed for opening some Surface bonds before the next layer is deposited**.**

3.2.5. Cytop Over-clad Spin Coating

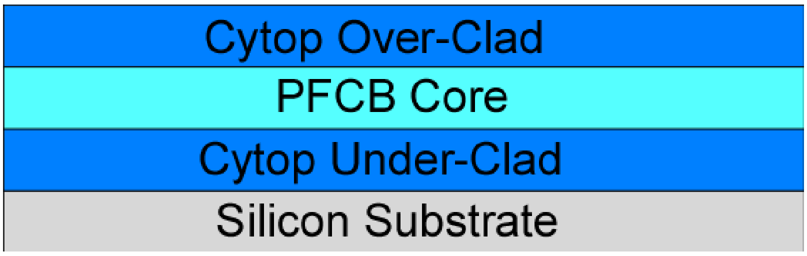

When we try to deposited 200nm oxide layer as hard mask on the PFCB layer problems occurred with oxide (~0.5 ppm/C^o) mask from stress [28], likely due to CTE mismatch with the polymer as we can see in figure 3.2.According to ref. [28] there is a built in stress in the PFCB (~60 ppm/C^o) film as a result of its coefficient of thermal expansion (CTE) mismatch with silicon substrate. This makes the film vulnerable to abrupt temperature change. Simulations with Comsol Multiphysics of a 20μm radius cross section at a 100^0 were preformed. The results are shown in figure 3.3 where we can clearly see that the stress are concentrated at the 200nm oxide layer. When I added 1.5μm Cytop layer the simulation show 10% decrease in the 200nm oxide layer stresses. The Cytop (~74 ppm/$C^{o)}$ was spun coated in 3000 rpm for duration of 30 second to achieve 1.5μm layer and then cured in oven set to 120^0 for duration of 4 hours.

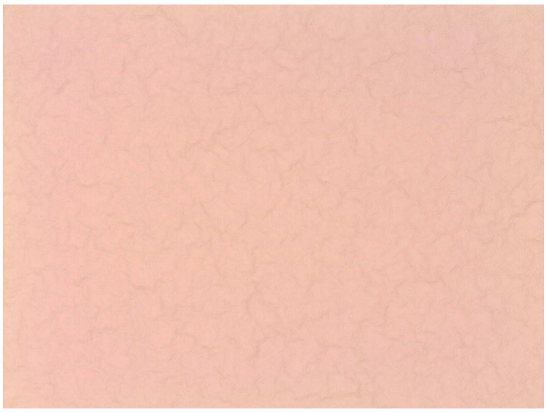

Figure 3.2: Microscope picture of cracks after deposition of 180nm oxide layer.

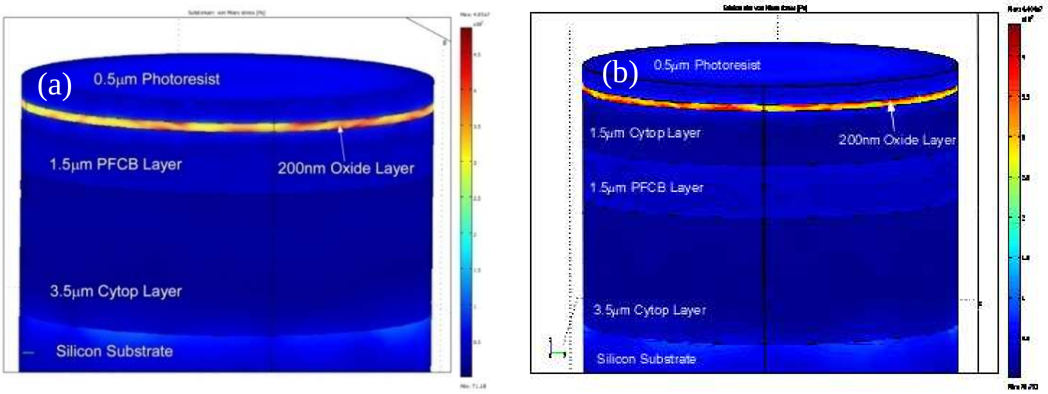

Figure 3.3: Comsol Simulations at 100^0 of a 20µm radius wafer cross section. (a) Without Cytop layer the maximum stress is 4.85×10^7 Pa. (b) With Cytop layer the maximum stress is 4.4×10^7 Pa.

3.2.6. 200nm oxide hard mask deposition

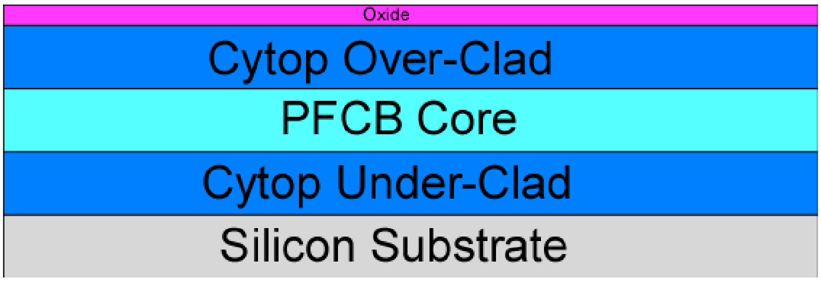

In the process of etching the waveguide channels by reactive ion etching (RIE) it is necessary to provide a mask material that has different sensitivity for the etching chemistry (Selectivity), this element is referred as a hard mask. Since the photoresist is also an organic polymer the etching rate of Cytop and the PR are at the same region, it is impossible to achieve the desire aspect ratio with the use of a PR mask at the RIE process. I chose as a hard mask material 200nm silicon dioxide (oxide) deposit in low temperature of 40^0 with CVD at a rate of 60nm/min with 4 mtorr chamber pressure and 40 sccm N_2O and 16 sccm SiH_4 flow rates for a duration of 3 minute as we can see in figure 3.4. When I deposit in higher temperature problem occur in the form of crack because of the thermal expansion mismatch between the oxide and the Cytop layer.

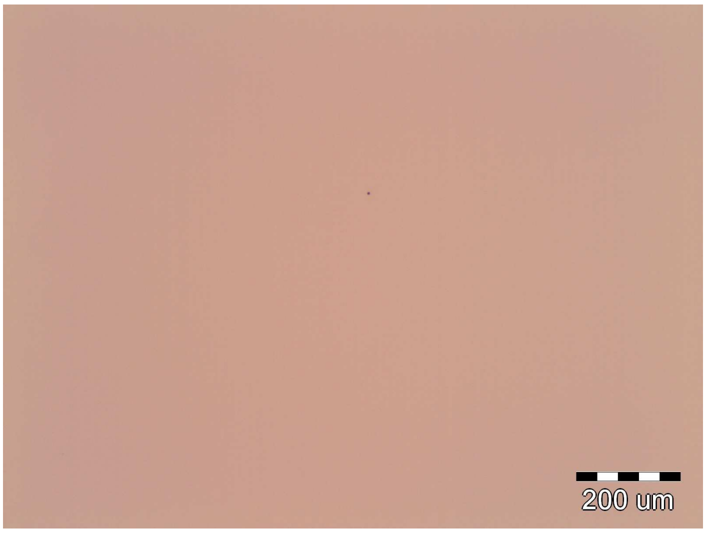

Figure 3.4: Microscope image 200nm oxide layer deposit at 40^0.

3.2.7. Lithography – PR Spin-coat, Prebake, Exposure, and Develop

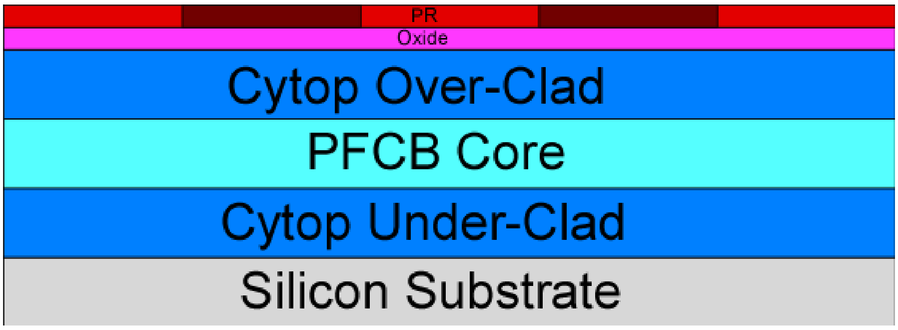

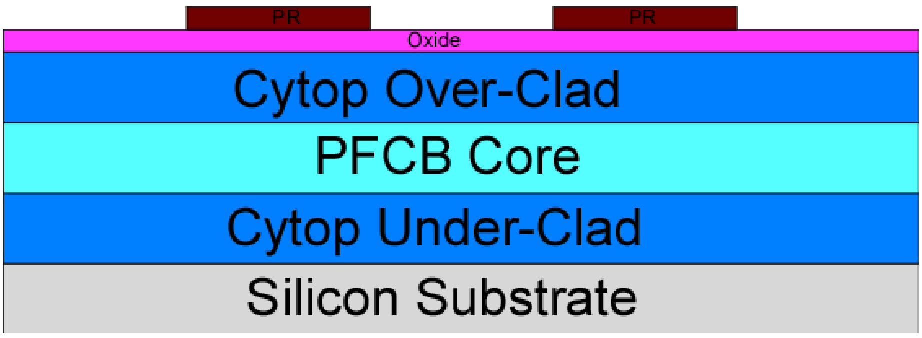

To achieve thin layers of 0.5um an AZ1505 photoresist was used. The application of AZ1505 allows for small resolution elements. Prior to spun coating of the photoresist the wafer was cured in a hot plate set to 100^0 for duration of 3 minute in order to remove humidity, this step is necessary to help the next polymer adhesion to succeed. The photoresist was spun coated in two steps: The first was in 600 rpm for duration of 7 second in a ramp level 3 in order to spread the photoresist on the wafer, the second was in 4000 rpm for duration of 30 seconds in a ramp level 3 to achieve the $0.5\mu m$ desire photoresist layer. Afterward the photoresist was cured in a hot plate set to 100^0 for duration of 10 minutes. The following step the wafer was placed in the lithography SUSS mask aligner, I set the parameters to a vacuum contact and 1 sec UV exposed time. The following step the wafer was placed in a developer (AZ 726 Developer) for duration of 15 seconds. Afterward I used to cure the developed photoresist layer on a hot plate at 100^0, but this step led to cracks in the wafer as we can see in figure 2.5, the solution was to cancel the step.

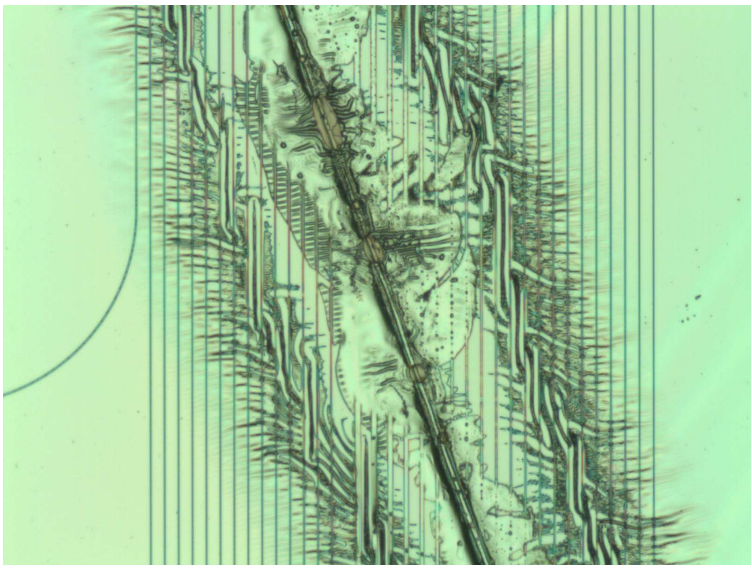

Figure 2.5: Microscope image of cracked after post-back the wafer in 100^0 for 10min.

3.2.8. Reactive Ion Etching (RIE)

3.2.8.1. Step 8a –Oxide Reactive Ion Etching (RIE)

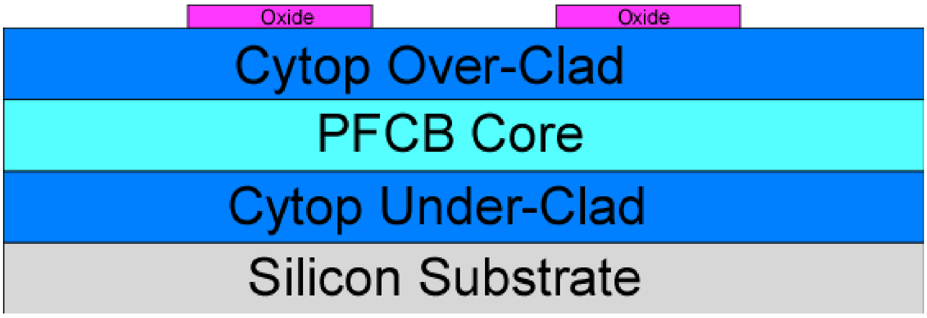

The process was done with an ICP-RIE Oxford Instruments Plasmalab System 100 plasma etcher machine. We etch the selective oxide layer at 15 mtorr chamber pressure and 50 sccm CHF_3 and 50 sccm Ar flow rates at 20° with results in etching rate of 60nm/min.

3.2.8.2. Cytop and PFCB RIE

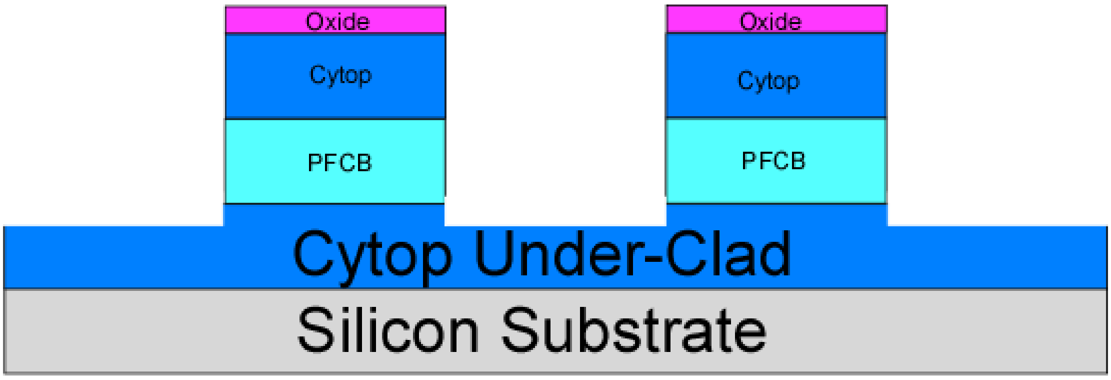

I etch the selective PFCB and Cytop layers at 2 mtorr chamber pressure and 10 sccm O_2 at 20°, which gives an etching rate of 1.704 $\mu m/\min$ for the Cytop and 0.717 $\mu m/\min$ for the PFCB and. Figure 3.6 shows a SEM picture (prior to final cladding spin-coating) of a fabricated device after the Cytop and PFCB etch process.

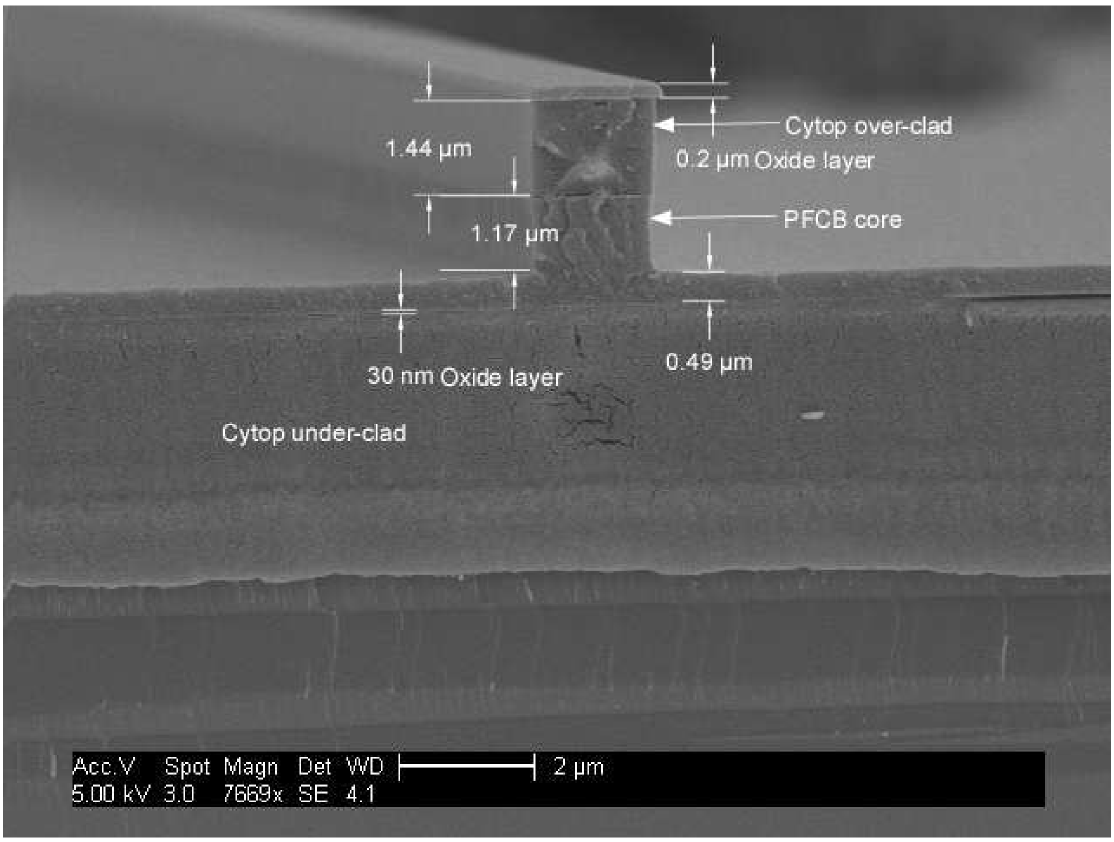

Figure 3.6: SEM Image of ridge waveguide with cross section of 1.66µm X 1.8µm after RIE process prior to final cladding spin-coating.

It is important that roughness of the WG sidewalls will by as small as possible for minimum optical losses. In this process the sidewalls roughness are in the 75nm scale as we see in figure 3.7. In ref. [28] the authors suggest that experiments can be done for roughness reduction by possibly reducing CO in the mixture that results in less sidewall passivation and therefore possibly less roughness.

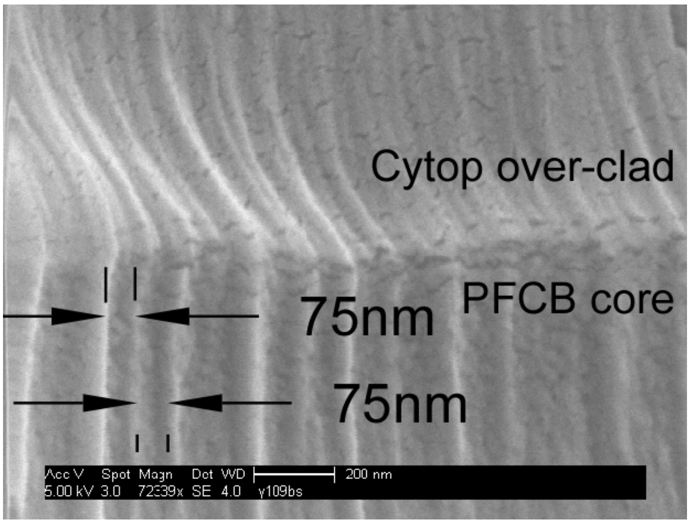

Figure 3.7: waveguide sidewall roughness on the 75nm scale.

After step 8 and 9 the waveguide width was 0.55-0.65μm narrowed as we can see in figure 3.8. This narrowing occurs because of the light exposure and development in the lithography Step and the RIE process. In order to reduce narrowing effect in [29] the authors report the successful development of a PFCB etch using a CO/O2 etch chemistry in an ICP RIE. The addition of CO purportedly promotes the development of a thin passivation layer on the sidewalls to suppress spontaneous chemical etching by oxygen and thereby prevents excessive trench widening. This narrowing should be considered in the mask design to get the required waveguide width.

Figure 3.8: Microscope image of 9, 8, 7μm waveguide width after step 8 from right to left.

3.2.8.3. Oxide RIE

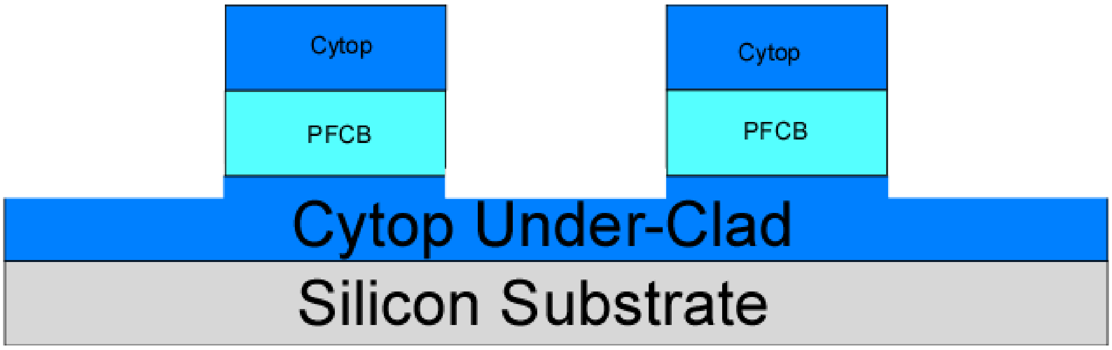

We etch the remaining oxide layer in the same condition as step 8a.

3.2.9. Cytop Overall Coating

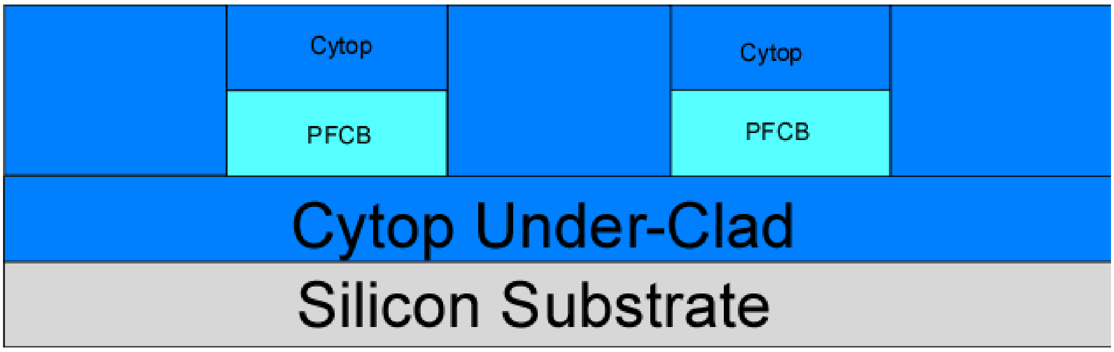

To produce symmetric signal wave mode in the waveguide, it is necessary that the core will be covered with the same refractive index material from all sides. Moreover it is essential to protect the waveguides channels from moisture, dust, or other physical damage, and to improve the long-term stability, the addition of a cladding layer is essential. A simple spun-coat and curing same as in step 2 was done. At the end of the curing it is seen that the Cytop layer had an adhesion problem with the devices as we can see in figure 3.9.Another problem is the solvent incompatibility between Cytop and PFCB that cause an undesired sidewall etch as we can see in figure 3.10. In order to solve those problems I deposited an oxide layer in the same way as step 3. At the end of curing at 120^0 for duration of 4 hours some devices were cracked. This problem occur because of the thermal expansion mismatch between the oxide and the Cytop layer, it was solve by lowering the curing temperature to 100^0 for duration of 2 hours.

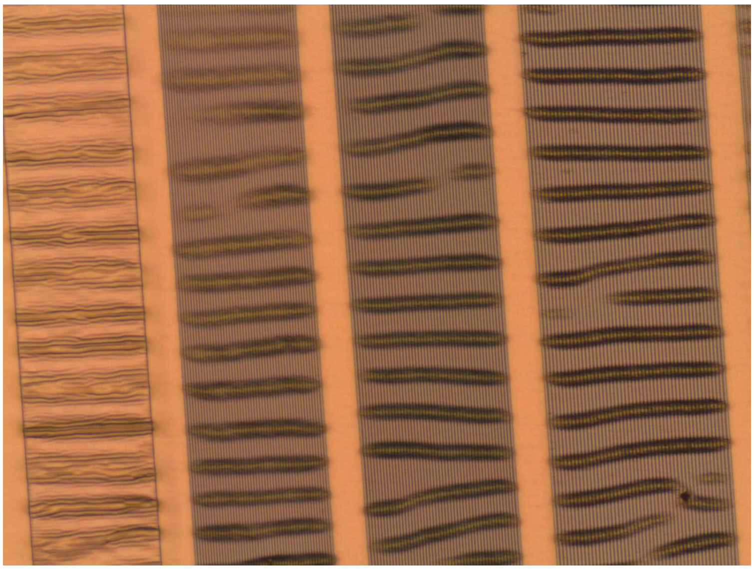

Figure 3.9: Microscope image of Cytop over-clad layer with an adhesion problem.

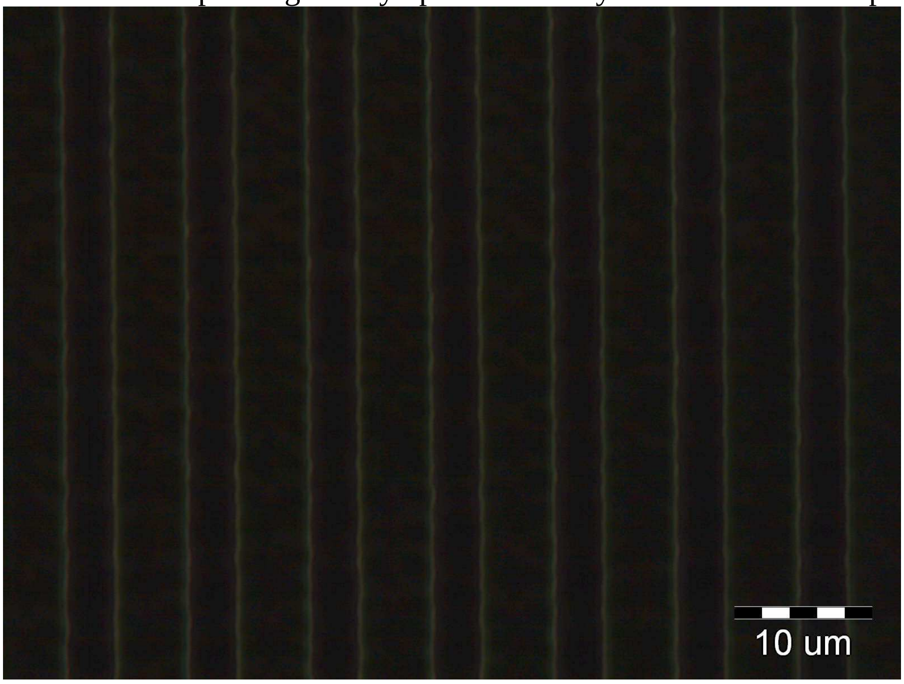

Figure 3.10: Dark field Microscope image of an undesired sidewall etch.

3.2.10. Gluing the cover glass

In order to access the WG we needed to dice the wafer and follow with edge polishing of edge. To withstand both the dicing and polishing, it was essential to cover the wafer with a glass substrate (200nm). In order to achieve this goal numbers of method were tested:

The first method was by spun coating 2μm film thickness of Cytop on both the wafer and the cover glass (200nm); afterwards they were attaching together and were cured at 120^0 for 2 hours. We can observe in figure 3.10 that a complete destruction of the WG has occurred during the curing process, reason being is that solvent for the Cytop was unable to evaporate.

In order to solve the problem we place both the wafer and the cover glass on a hot plate at 50^0 for 2 minute in an attempt of removing the solvent, and then they were attached together and were cured at 120^0 for 2 hours; the result was an improvement but still some solvent damage could be observed. In an a attempted of protecting the wafer from the solvent damage we deposit 200nm oxide layer, it solved the solvent damage but when we attempted to dice the wafer the cover glass disconnected from the wafer.

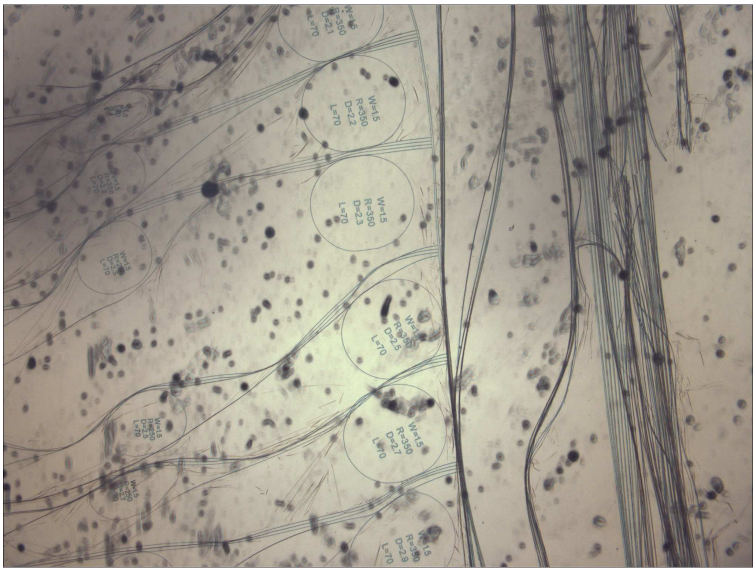

Figure 3.10: Microscope image of the complete destruction of WG after the curing process.

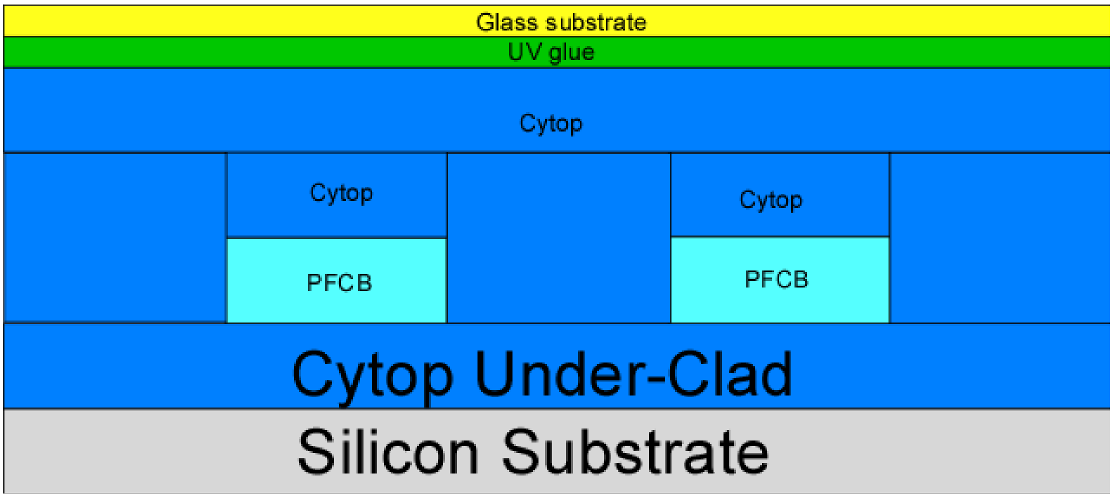

The second method we cover the wafer with a glass substrate that has been glued with a thin layer of UV adhesive. Short O2 plasma etching surface treatment of 30 second was carried out followed by spin coating of 4μm film thickness of Cytop that was cured at 100^0 for 1 hour (The second Cytop layer function is to insure 4μm clad in any direction as the simulation required); Second O2 plasma etching surface treatment of 30 second was carried out followed by spin coating ((1) 600rpm for 7 second in a ramp level 3 (2)1000rpm for 30 seconds) of a thin layer of UV glue (Norland optical adhesive 61).In order to achieve as thin layer as possible the wafer and the cover glass were squeezed by hand and was put in a mask-aligner for 20 seconds UV exposed time. The final result was a 14μm UV glue layer as we can see in figure 3.11.

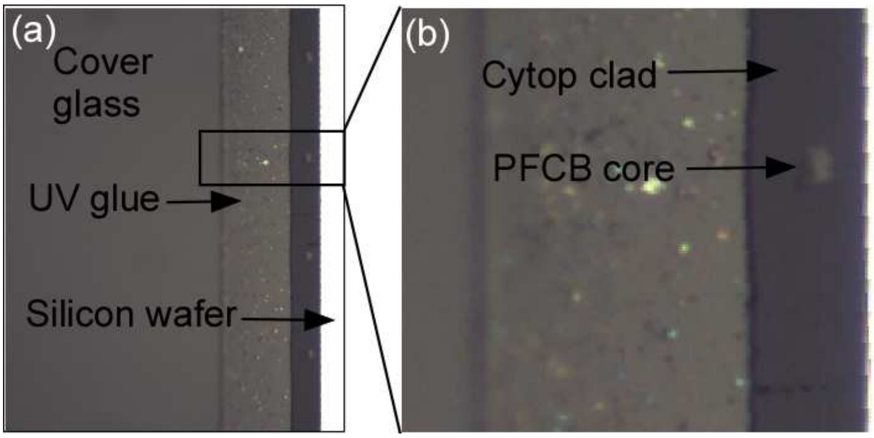

Figure 3.11: (a) Microscope Image of diced edge polish part. (b) Magnified image of a PFCB core with waveguide cross section of 1.5μm×2μm.

3.2.11. Dicing

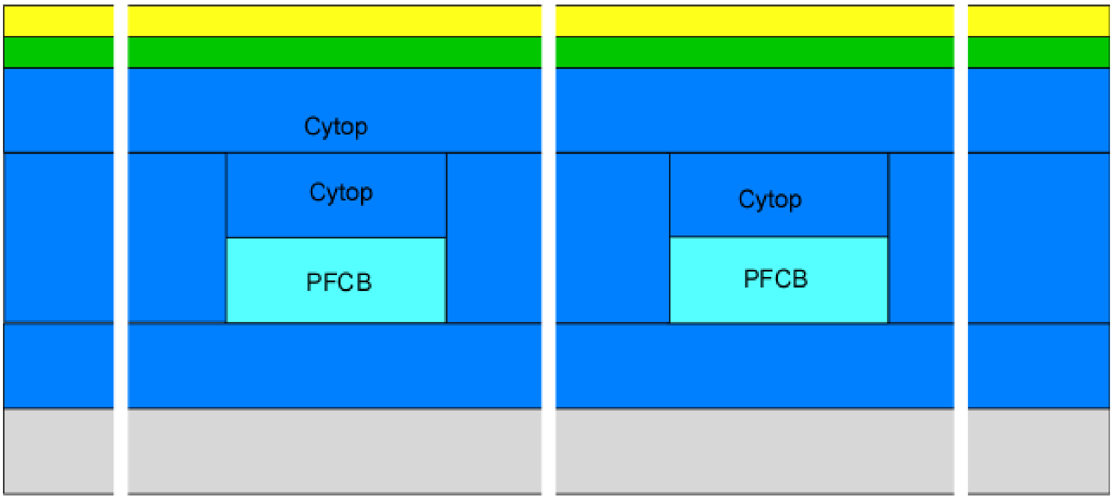

Dicing is an important step that exposes the input and output waveguide faces for in and out coupling of light once waveguide devices are fabricated on the substrate. The dicing was done using with a diamond saw speed of 1.5mm/sec.

3.2.12. Polish

Polishing the edges is done in seven steps of polishing sheets from 15μm to 0.1μm. Figure 3.11 shows a polished silicon wafer with the polished PFCB core.

4. Optical Waveguide Characterization

4.1. Introduction

The characterization of fabricated optical waveguides is a very important and essential step in any waveguide fabrication process. It is necessary to evaluate and to confirm that the fabricated waveguide exhibits characteristics as designed. Some of the waveguide parameters that are usually measured are: the waveguide transmission loss, bend loss and mode profiles. The evaluation of the waveguide characteristics serve as a feedback to the design and the fabrication process, which is crucial for the improvement of the waveguide performance. In this chapter, the various optical waveguide characterization techniques used in this dissertation will be elaborated.

4.2. Imaging the radiated light at the output facet

The experimental setup is shown in figure 4.1. Our light source was HP 8168F Tunable Laser Source tuned at wavelength of 1.55μm (output of 0dBm) which was launched into a lens fiber (polarization maintaining fiber with tapered tip on one end, spot diameter of 2.5±0.25μm, working distance 14±2 μm) and coupled into the input of the waveguide facet.

The exit facet of the waveguide was imaged with a 50× objective (Mitutoyo Plan Apo NIR Infinity-Corrected with NA=0.42, working distance of 17mm and resolving power of 0.7μm).The transmitted light was than focus using f=200mm tube lens onto the target IR camera (SU320-1.7RT). The sample, lens fiber and camera were mounted on high precision xyz stages to achieve accurate and stable alignment.

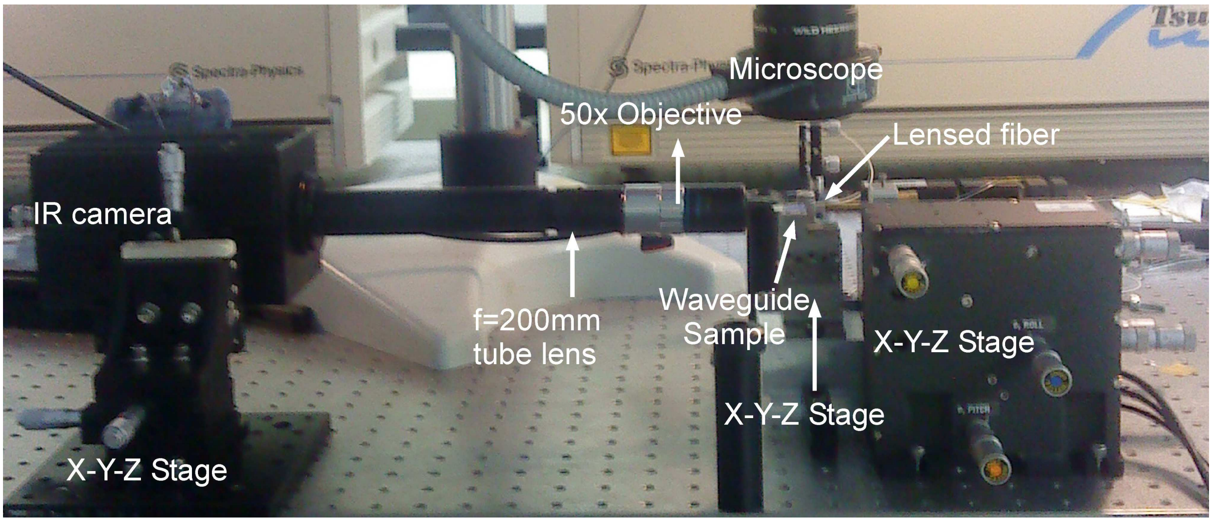

Figure 4.1: The experimental setup for imaging the radiated light at the output facet.

Figure 4.2a shows the measured guided mode size from 1.5µmX1.5µm square waveguide at wavelength of 1.55µm. We obtain a Gaussian fit mode size height of $2\omega_0$=2.75±0.4µm and width of $2\omega_0$=2.88±0.42µm as shown in figure 4.2b. To verify our results we compared it to a simulation for a waveguide with the same parameters as shown in figure 2.5 .The result obtained from figure 2.5 result in a waist of 1.88µm, which is not in good agreement with our experimental result. The reason for the discrepancy is the numerical aperture mismatch between the waveguide output facet NA=0.5 and the 50× objective NA=0.42.In order to solve the problem we can use objective with larger NA.

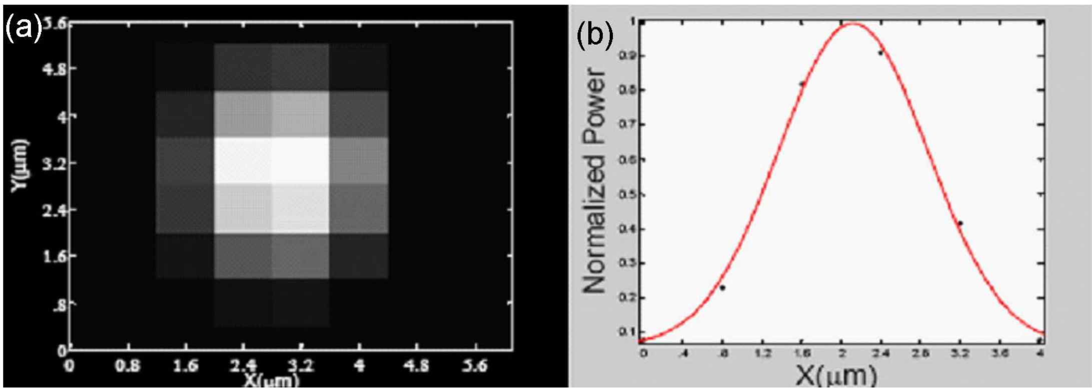

Figure 4.2: (a) Image of waveguide output with dimensions of 1.5µm X1.5µm. (b) Intensity profile with Gaussian fit which gives width of $2\omega_0$=2.88±0.42µm.

4.3. Propagation Loss Measurements

Waveguide propagation loss measurements were performed using a Lightwave Measurement System agilent HP 8164A. A polarizer had been used for adjusting the light polarization for both TE and TM guided mode .The laser beam was launched into a lens fiber and coupled into the input of the waveguide facet. The output waveguide facet power was coupled into lens fiber and then was measurement using lightwave multimeter. The sample and lens fiber were mounted on high precision xyz stages to achieve accurate and stable alignment. The experimental setup is shown in figure 4.3.

In figure 4.4 we can see the interference fringes of a Fabry-Perot cavity spectrum for waveguide with square core dimensions of 1.5µmX1.5µm and waveguide length of 0.851cm.Using Eqs. 2.8, 2.10 we receive propagation loss of 1.06dB/cm at 1.55µm wavelength. For 0.85µmX1.5µm waveguide we receive propagation loss of 3.48dB/cm at 1.55µm wavelength.

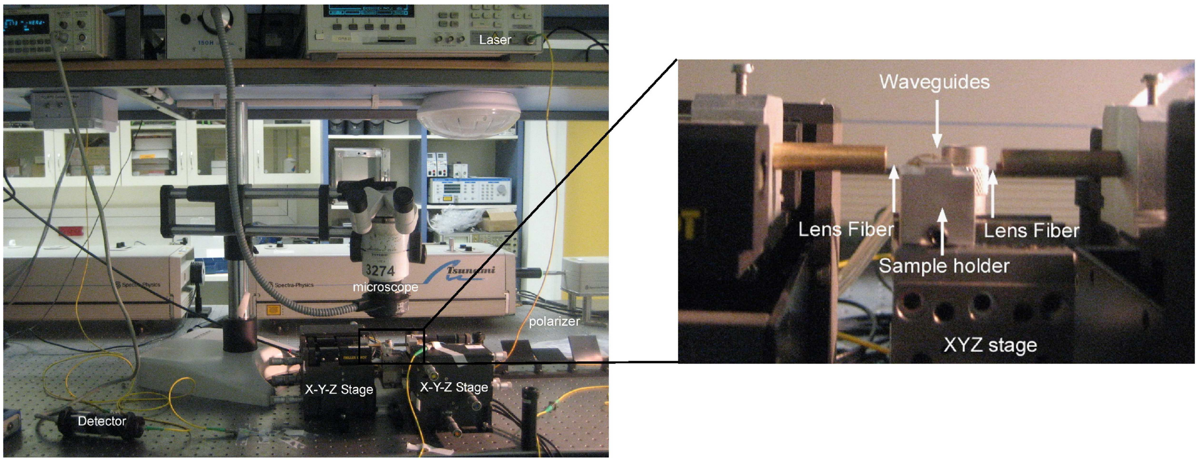

Figure 4.3: The experimental setup for propagation loss measurements.

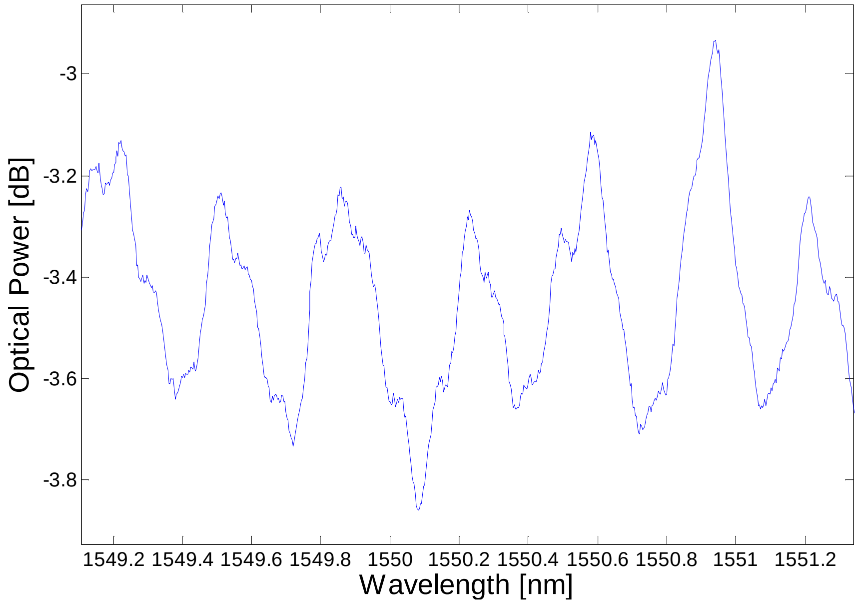

Figure 4.4: Fabry-Perot cavity spectrum for waveguide with core dimensions of 1.5µmX1.5µm.

Propagation losses of the fabricated waveguides are higher than the theoretical value (0.29dB/cm) because of the interaction between the mode in the waveguide and the sidewall roughness and fabrication imperfections of the channel waveguides.

Measurements using the cutback Method with waveguides of different lengths indicate that coupling losses dominate over propagation losses. In order to overcome this problem we need to design waveguides with larger length which will result in propagation losses which are dominate over the coupling losses.

4.4. Bend Loss Measurements

Waveguide bend loss measurements were preformed using the same experimental setup as presented at figure 4.3. The fabricated racetrack resonators which were tested had core dimensions of 0.85μmX1.5μm as opposed to our 1.5μm×1.5μm target because of the waveguides narrowing at the etching stage (see chapter 3). This outcome made the tested racetrack resonators more sensitive to the sidewall roughness, therefore made the bend loss dominate over the propagation loss in the ring cavity.

In figure 4.5 we can see microscope image of fabricated racetrack resonator and in

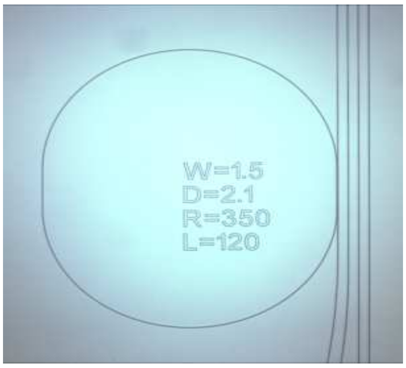

Figure 4.5: Microscope image of fabricated racetrack resonator with radius 350μm and coupler separation 2.1μm.

figure 4.6 we can see the optical spectrum of the device which gave critical coupling at 1.553μm and deepest dip of -18dB. We also see the interference fringes at -3dB; these oscillations are related to different propagation constants for different polarizations. In figure 4.7 we can see the same interference fringes at straight waveguides with different length and different polarization state. We can see that the 6nm fringes period staying constant regardless of the polarization state or waveguide length; only the interference fringes phase changes depending on the polarization state. In figure 4.8 we can see theoretical response curves and comparison with experiments which gives Quality-factor of 22000 and finesse of 9.56.

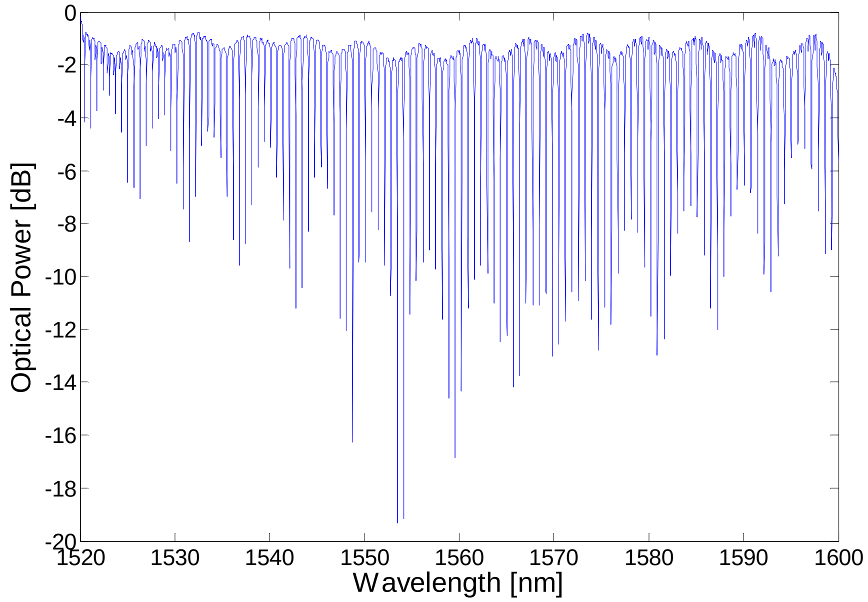

Figure 4.6: Resonance spectrum for a racetrack resonator (shown in figure 4.5) with cavity length of 2.24 mm.

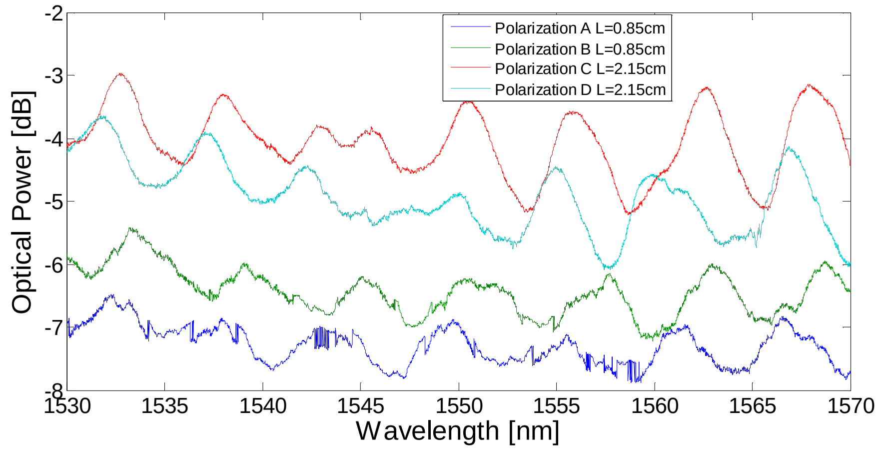

Figure 4.7: Interference fringes at straight waveguides with different length and different polarization state.

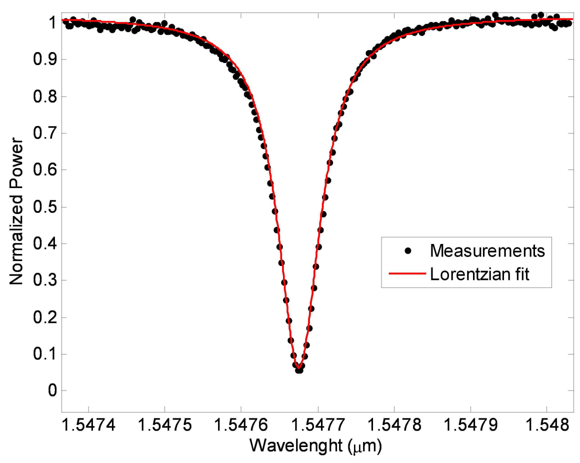

Figure 4.8: Comparison of theoretical and measured responded at one wavelength from figure 4.

In order to separate between t'^2 and α'^2 I used the technique described in **2.6.1.3**.The extracted values are assigned as α'^2 or t'^2 relying on the fact that α'^2 should be similar for Rings with radius bend R=350μm but with different couplers. In figure 4.9 we can see the extract parameters α'^2 and t'^2 as a function of wavelength for rings with different coupler separation 2.2μm and 2.5μm. We can see that the loss factor α'^2 is similar and t'^2 is different as expected and varies approximately sinusoidally with wavelength [20].Using Eq. 2.39 I received 0.25dB/90^0 (4.27dB/cm) bend loss at 1.55μm wavelength.

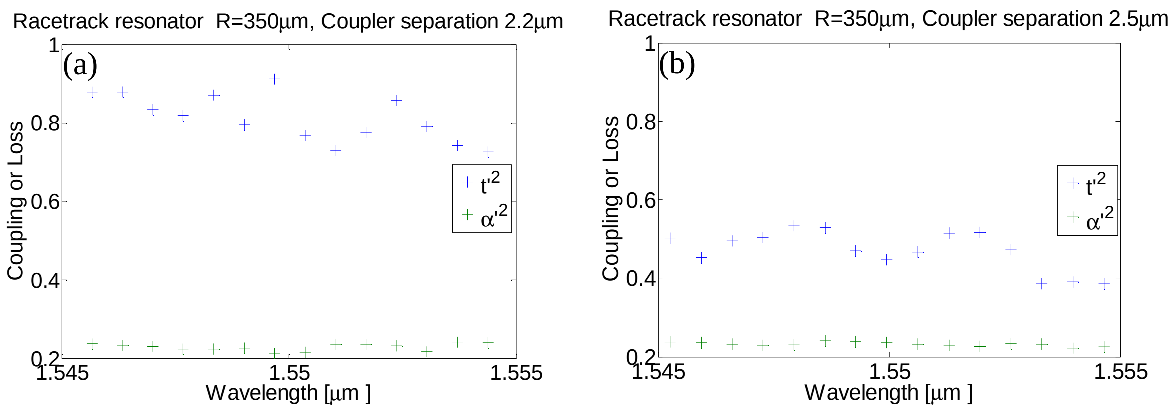

Figure 4.9: Self-coupling coefficient t'^2 (green plus sign) and loss coefficient α'^2 (blue plus sign) for the resonators with R=350μm radius bend. (a) Racetrack resonator with coupler separation 2.2μm. (b) Racetrack resonator with coupler separation 2.5μm.

Figure 4.10 shows the transmission spectra for racetrack resonator from Figure 4.8a, with an FSR of 0.678 nm at 1.55 nm wavelength and n_g of 1.514. The FSR is defined by Eq. (4.1) [30]:

$$FSR = \left| \frac{\lambda^2}{n_g \cdot L} \right| \tag{4.1}$$

where n_g is the effective group index and L is the racetrack resonator cavity length. Using Eq.2.3 we receive calculated n_g of 1.467 with result in calculated FSR of 0.699nm.The difference between the measured and calculated result is the result of fabrication imperfections of the channel waveguides.

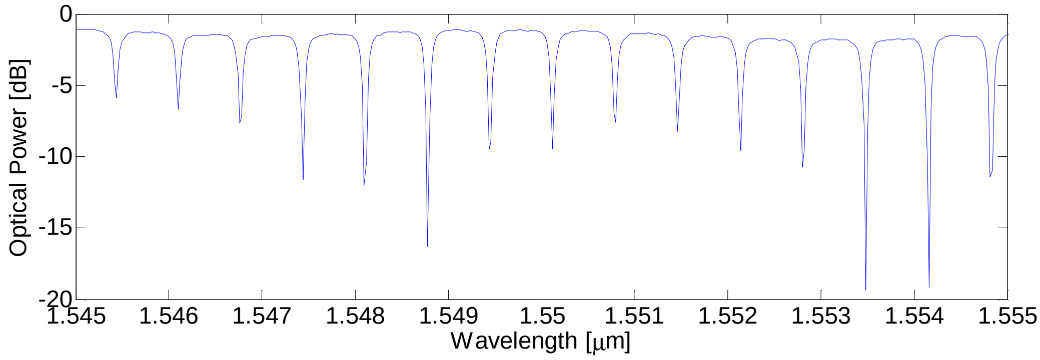

Figure 3.10: Transmission spectra of racetrack resonator with coupler separation 2.2μm, R=350μm, cavity length of 2.24 mm and a FSR of 0.678 nm at 1.55μm wavelength.

In figure 3.11 we can see the extract parameters α'^2 as a function of wavelength for racetrack resonator with different coupler separation 2.1μm and 2.3μm and bend radius of 250μm. We can see that the loss factor α'^2 is similar as expected. Using Eq. Eq. 2.38 I received 0.23dB/90^0 (5.37dB/cm) bend loss for TM polarization at 1.55μm wavelength (coupler with separation of 2.1μm) and 0.2dB/90^0 (4.67dB/cm) bend loss at TE polarization. Experimental results showed that the losses of the TE mode are smaller than the TM mode. This result directly demonstrates that the main source of propagation losses in our waveguides is the residual surface roughness on the etched sidewalls. Indeed, as it is seen from figure 2.5, the TM mode profile is characterized by much higher electric field intensity at the sidewalls and correspondingly higher propagation losses. In contrast, the TE mode has a relatively small amplitude at the sidewalls, but much higher at the top and bottom interfaces.

Figure 4.12 shows the transmission spectra for TM (a) and TE (b) polarizations for racetrack resonator with coupler separation 2.1μmand radius bend of 250μm.The FSR for the TE and TM is 0.92nm which is in a good agreement with the calculated results and n_g of 1.51.

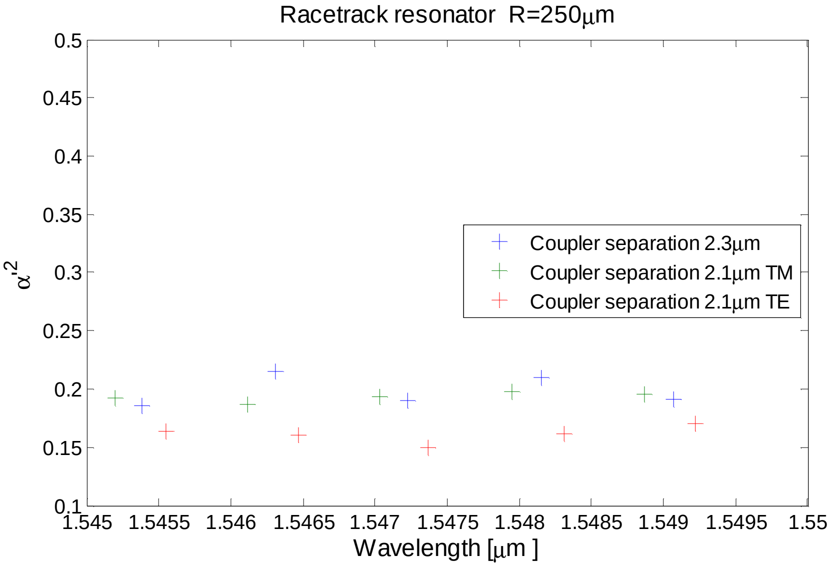

Figure 4.11: Loss coefficient α'^2 for the racetracks resonators with R=250μm radius bend. Blue plus sign is resonator with coupler separation 2.3μm. Green plus sign is resonator with coupler separation 2.1μm with TM polarization. Red plus sign is resonator with coupler separation 2.1μm with TE polarization.

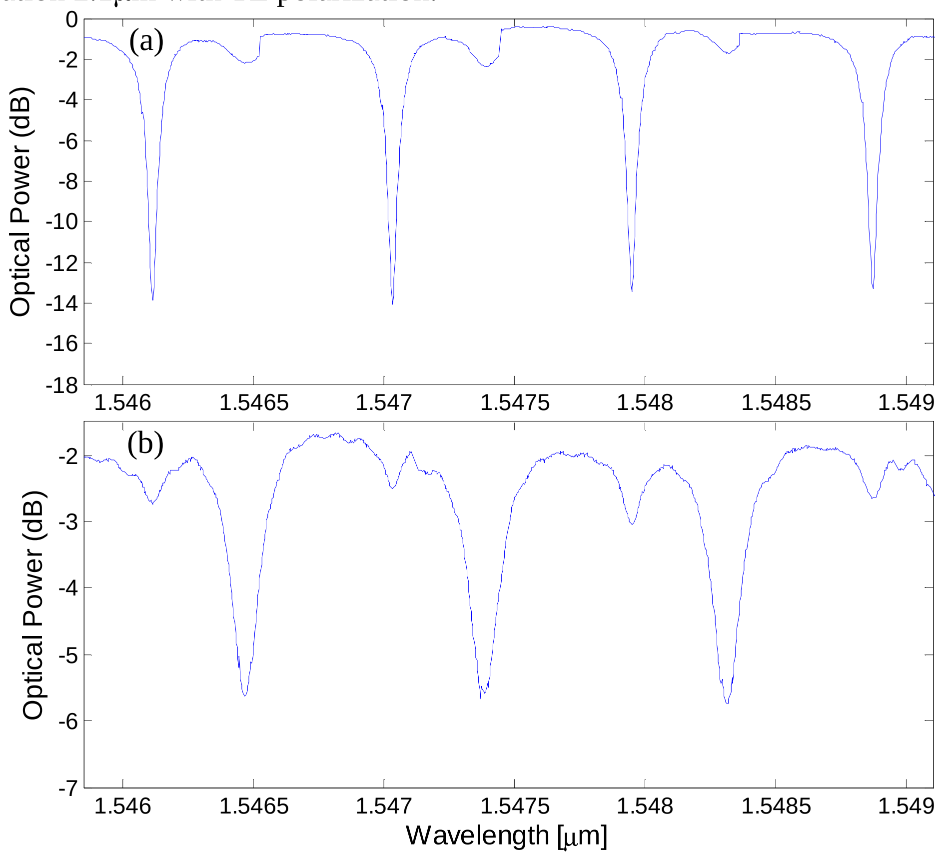

Figure 4.12: Transmission spectra for TM (a) and TE (b) polarizations for racetrack resonator with coupler separation 2.1μm, R=250μm, cavity length of 1.71 mm.

For waveguides with radius bend of 150μm I received 0.27dB/90^0 (9.97dB/cm) bend loss for TE polarization at 1.55μm wavelength and 0.6dB/90^0 (22.17dB/cm) bend loss for

TM polarization. For waveguides with radius bend of 100μm I received 0.37dB/90^0 (19.26dB/cm) bend loss for TE polarization at 1.55μm wavelength. We can see that for higher bend radius the losses are higher as expected.

Since the other factors such as sidewall roughness can have significant effects on losses in sharp waveguide bends, it was not expected that measured waveguide performance would match theoretical expectations based on the loss associated with propagating modes in idealized waveguides.

Measurements using the bend loss array indicate that coupling losses dominate over bend losses. In order to overcome this problem we need to design bend loss array with more 90^0 bends which will result in bend loss that are dominate over the coupling losses.

5. Conclusion

5.1. Chapter by Chapter Conclusion

Chapter 2 has presented the parameters selection for the high index waveguide. I calculated that the cut-off core dimensions criteria for single mode waveguide is 1.5µm width and height and showed that for 3.5µm Cytop under-cladding layer the substrate leakage is negligible.

Chapter 3 summarized the process development for polymer waveguiding materials based on PFCB and Cytop. The process development was the main contribution of my time effort which proved to be more challenging than expected. In order to solve those process challenges I developed unique solutions such as introducing nanometric chemical vapor deposition as a coupling agent between the Cytop and PFCB, the deposition of thin oxide layer after the RIE stage in order to enhancing the coupling to the final Cytop cladding layer; Adding 1.5µm Cytop layer in order to decrease the CTE mismatch stress between PFCB and the 200nm oxide and the silicon substrate. Figure 5.1 describes the fabrication flow I developed for creating the polymer waveguides.

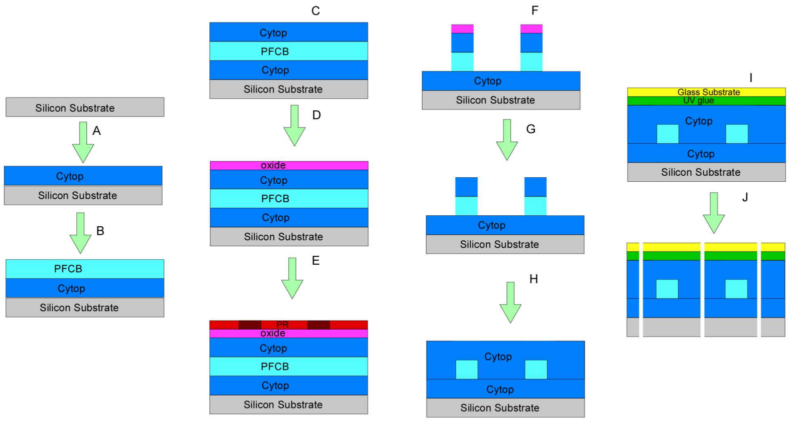

Figure 5.1: Process flow for fabricating polymer waveguides. A) Cytop Under-Clad B) PFCB Core C) Cytop over-Clad D)Chemical Vapor Deposition of 200nm Oxide E) PhotoResist (PR)PhotoResist Spin Coat, Prebake, Exposure, Develop F) Oxide Cytop and PFCB RIE G) Oxide RIE H) CVD of 30nm Oxide and then Cytop Over-clad.I)UV glued spin coat, Glass substrate, UV exposure J)Dicing ,and Polishing.

Chapter 4 summarized all of the experimental results on waveguide transmission losses and imaging the radiated light at the output facet. The measured mode size was $2\omega 0=2.95\pm 0.4\mu m$ which is not in good agreement with our numerical result. I measured the propagation loss using the Fabry–Perot resonance technique, which gave losses of 1.06dB/cm at 1.55μm wavelength for 1.5μmX1.5μm core dimensions. For 0.85μm X1.5μm waveguide I receive propagation loss of 3.48dB/cm at 1.55μm wavelength.

Propagation losses of the fabricated waveguides are higher than the theoretical value because due to sidewall roughness and fabrication imperfections of the channel waveguides. Measurements using the cutback method indicate that coupling losses dominate over propagation losses. In order to overcome this problem I need to design waveguides with larger length which will result in propagation losses which are dominate over the coupling losses.

Bend loss measurement was evaluated using racetrack resonators with different design parameters. I measured a bend loss of $0.25dB/90^0$ (4.27dB/cm) at 1.55μm wavelength for 350μm radius bend at an erroneous core dimensions of 0.85μm×1.5μm (as opposed to our 1.5μm×1.5μm target), which made the waveguide mode more sensitive to the sidewall roughness. We plan to resolve this problem by enlarging the core dimensions in the next mask design. For radius bend of 250μm I received $0.23dB/90^0$ (5.37dB/cm) bend loss for TM polarization at 1.55μm wavelength and $0.2dB/90^0$ (4.67dB/cm) bend loss at TE polarization. Experimental results showed that the losses of the TE mode are smaller than the TM mode. This result directly demonstrates that the main source of propagation losses in our waveguides is the residual surface roughness on the etched sidewalls.

5.2. Future Work

Semiconductor nanocrystals offer exciting properties that are determined by their composition, size, and shape, allowing for bandgap engineering of their discrete electronic level structure and optical transitions. Research in this field is very active due to the great potential offered by these chemically synthesized nanocrystals. However, when one wants to build functional devices that utilize the enhanced nanocrystal properties, then the interaction of a large ensemble of nanocrystals is involved. To fully exploit the favorable nanocrystal properties, it is advisable to control and align all (or most) of the nanocrystals, so that their properties project towards the ensemble instead of averaging over all possible orientations. We plan to investigate two promising techniques for alignment and fixation of semiconductor nanocrystals embedded within thin-film device layers of a polymer matrix host. The first alignment technique is based on an applied electric field. The second alignment technique is based on templated self assembly and is applicable to nanocrystals formed as nanorods.

References

1. Okamoto, K., Fundamental of Optical Waveguides. Optics and Photonics. 2000, San Diego: Academic Press
2. Bruchez M, Moronne M, Gin P, Weiss S, and Alivisatos AP, "Semiconductor nanocrystals as fluorescent biological labels", Science, 281, 2013, 1998.
3. S. Coe, W. K. Woo, M. G. Bawendi, and V. Bulovi, "Electroluminescence from single monolayers of nanocrystals in molecular organic devices", Nature (London) 420, 800, 2002.
4. V. I. Klimov, A. A. Mikhailovsky, S. Xu, A. Malco, J. A. Hollingsworth, C. A. Leatherdale, H.-J. Eisler, and M. G. Bawendi, "Optical Gain and Stimulated Emission in Nanocrystal Quantum Dots," Science 290, 314-317, 2000.
5. Klimov VI, Mikhailovsky AA, McBranch DW, Leatherdale CA, "Quantization of multiparticle auger rates in semiconductor quantum dots", Science 287 (5455), 1011, 2000.
6. Oron D, Kazes M and Banin U, "Multiexitons in Type-II Colloidal Semiconductor Quantum Dots", Phys. Rev. B 75, 035330 (2007).
7. O. Millo, D. Steiner, D. Katz, A. Aharoni, S. Kan, T. Mokari, and U. Banin, “Transition from zero-dimensional to one-dimensional behavior in InAs and CdSe nanorods,” Physica E 26, pp. 1-8 , 2005.
8. J. T. Hu, L. S. Li, W. D. Yang, L. Manna, L.W. Wang, and A. P. Alivisatos, “Linearly polarized emission from colloidal semiconductor quantum rods,” Science 292, pp. 2060-3, 2001.
9. Harrison MT, Kershaw SV, Burt MG, Rogach AL, Kornowski A, Eychmüller A, and Weller H, "Colloidal nanocrystals for telecommunications. Complete coverage of the low-loss fiber windows by mercury telluride quantum dots", Pure Appl. Chem., Vol. 72, Nos. 1–2, pp. 295–307, 2000.
10. J. Ballato, S. H. Foulger, D. W. Smith, “The Optical Properties of Perfluorocyclobutyl Polymers II: Theoretical and Experimental Performance,” *Josa B*, vol. 21, Issue 5, 2004, pp. 958-967.
11. M. T. Harrison, S. V. Kershaw, M. G. Burt, A. L. Rogach, A. Kornowski, A. Eychmüller, H. Weller, “Colloidal nanocrystals for telecommunications. Complete coverage of the low-loss fiber windows by mercury telluride quantum dots, “ Pure Appl. Chem., vol. 72, Nos1–2, 2000, pp. 295–307.
12. Y. K. Olsson, G. Chen, R. Rapaport, D. T. Fuchs, V. C. Sundar, J. S. Steckel, M. G. Bawendi, A. Aharoni, U. Banin, “Fabrication and optical properties of polymeric waveguides containing nanocrystalline quantum dots,” Appl. Phys. Lett. 85, 2004, pp. 4469-4471.
13. Zhao, Y.G., et al., Polymer waveguides useful over a very wide wavelength range from the ultraviolet to infrared. Applied Physics Letters, 2000. 77(19): p. 2961-2963.
14. Yaron Glazer, Dan M. Marom, Novel Polymeric Waveguides Optimized For Nanocrystals Hosting, M.Sc. Thesis 2009.
15. F. Ladouceur and J. D. Love, Silica-based Buried Channel Wave-guides and Devices. Chapman & Hill, 1996.
16. D. Jackson, Classical Electrodynamics. John Wiley and Sons, 3 ed.,1998.
17. P. K. Tien, "Light waves in thin films and integrated optics," Appl. Opt., 10, 2395 (1971)
18. G. Tittelbacht, B. Richter and W .Karthet," Comparison of three transmission methods for integrated optical waveguide propagation loss measurement," pure appl. Opt.,2,683 (1993)
19. K. Junguji, M. Horiguchi, T. Manabe, Appl. Opt. 21 (1982) 571.

20. W. R. McKinnon, D.-X. Xu, C. Storey, E. Post, A. Densmore, A. Delage, P. Waldron, J. H. Schmid, and S. Janz," Extracting coupling and loss coefficients from a ring resonator" Optical express vol. 17, no. 21 (2009).
21. A. Yariv, "Universal relations for coupling of optical power between microresonators and dielectric waveguides," Electron. Lett. 36, 321-322 (2000).
22. G. Gupta, Y.-H. Kuo, H. Tazawa, W. Steier, A. Stapleton, and J. O'Brien, "Analysis and Demonstration of Coupling Control in Polymer Microring Resonators Using Photobleaching," Appl. Opt. (to be published).
23. L. F. Stokes, M. Chodorow, and H. J. Shaw, "All-single-mode fiber resonator," Opt. Lett. 7 288-290 (1982).
24. S. Xiao, M. H. Khan, H. Shen, and M. Qi, "Modeling and measurement of losses in silicon-on-insulator resonators and bends," Opt. Express 15, 10553-10561 (2007).
25. Doerr, C.R. and H. Kogelnik, Dielectric waveguide theory. Journal of Lightwave Technology, 2008. 26(9-12): p. 1176-1187.
26. Dragone C, "Optimum Planar Bends" Electronics letters, Vol. 29 No. 29 pp. 1121-1122, 1993.
27. T. K. Lim, B. K. Garside, J. P. Marton, "An Analysis of Optical Waveguide Tapers" Applied Physics, Vol. 18, pp. 53-62, 1979.
28. NAZLI RAHMANIAN, high efficiency perfuorocyclobutyl air–trench splitters for use incompact ring resonator.
29. Seunghyun Kim and Gregory P. Nordin , Anisotropic high aspect ratio etch for perfluorcyclobutyl polymers with stress relief technique, *J. Vac. Sci. Technol. B* **24**, pp. 2672-2677.
30. D. G. Rabus and M. Hamacher, "MMI-coupled ring resonators in GaInAsP-InP", IEEE Photon. Technol. Lett., vol. 13, pp. 812 - 814, 2001.